Commun. Comput. Phys.
doi: 10.4208/cicp.230914.040615a

Vol. **19**, No. 2, pp. 496-533
February 2016

Development of a High-Resolution Scheme for Solving the PNP-NS Equations in Curved Channels

Tony W. H. Sheu[1,2,3,*], Yogesh G. Bhumkar[2,4], S. T. Yuan[1] and S. C. Syue[1]

[1] *Department of Engineering Science and Ocean Engineering, National Taiwan University, Taipei, Taiwan, 10617.*
[2] *Center of Advanced Study in Theoretical Sciences (CASTS), National Taiwan University, Taipei, Taiwan, 10617.*
[3] *Institute of Applied Mathematical Sciences, National Taiwan University, Taipei, Taiwan, 10617.*
[4] *School of Mechanical Sciences, IIT Bhubaneswar, Odisha, India, 751013.*

Communicated by Chi-Wang Shu

Received 23 September 2014; Accepted (in revised version) 4 June 2015

Abstract. A high-order finite difference scheme has been developed to approximate the spatial derivative terms present in the unsteady Poisson-Nernst-Planck (PNP) equations and incompressible Navier-Stokes (NS) equations. Near the wall the sharp solution profiles are resolved by using the combined compact difference (CCD) scheme developed in five-point stencil. This CCD scheme has a sixth-order accuracy for the second-order derivative terms while a seventh-order accuracy for the first-order derivative terms. PNP-NS equations have been also transformed to the curvilinear coordinate system to study the effects of channel shapes on the development of electroosmotic flow. In this study, the developed scheme has been analyzed rigorously through the modified equation analysis. In addition, the developed method has been computationally verified through four problems which are amenable to their own exact solutions. The electroosmotic flow details in planar and wavy channels have been explored with the emphasis on the formation of Coulomb force. Significance of different forces resulting from the pressure gradient, diffusion and Coulomb origins on the convective electroosmotic flow motion is also investigated in detail.

AMS subject classifications: 76D05, 76D55, 65M06, 65M22

Key words: PNP, NS, five-point stencil, combined compact difference, electroosmotic flow, Coulomb force.

*Corresponding author. *Email addresses:* twhsheu@ntu.edu.tw (T. W. H. Sheu), bhumkaryogesh@gmail.com (Y. G. Bhumkar), r99525055@ntu.edu.tw (S. T. Yuan), r02525068@ntu.edu.tw (S. C. Syue)

 ©2016 Global-Science Press

https://doi.org/10.4208/cicp.230914.040615a Published online by Cambridge University Press

1 Introduction

Design of a microfluidic biochemical device to propel ionic fluids from one end to the other end has been an important research topic [1]. For an effective control of flow motion to enhance fluid mixing and to avoid flow separation, the concept of miniaturized total analysis (μTAS) proposed in the early 1990s [2] can be adopted. With the remarkable progress in μTAS, today biochemical analysis has many applications in the fields of microfludics and display [3]. One can refer to [4] for an overview of applications of magnetohydrodynamics to DC/AC electrokinetics for electroosmotic or electrophoresis/dielectrophoresis flow. The techniques exploiting the physicochemical properties of solid-electrolyte interface are referred as electroosmotics [5].

Electroosmotic flow (EOF) results from a motion of accumulated electric charges on the no-slip surfaces which are in contact with electrolyte solution. These ions are accumulated in a thin layer immediately close to the wall. This thin layer is also known as the electric double layer (EDL) or Debye layer [6]. Electrolyte away from this thin layer is neutral. Charge separation near the solid surface establishes a positive or a negative potential difference across the Debye layer. When an external electric field is applied, the counter ions in the Debye layer are attracted to the oppositely charged electrodes. Motion of these ions induces fluid flow. In other words, the electric force can be exploited as the leading factor to drive and control the movement of operating fluid and the charged species. For example, motion of beads and pigmented particles of the size ranging from a sub-millimeter to a few microns in electrode-bounded channels can be controlled using the above mechanism.

In microfluidic devices the gap between electrodes is very small and one can easily generate a highly localized and large electric field. For such devices, electric force can be used precisely for flow control. Microfluidic devices are normally featured with a much larger surface-to-volume ratio in comparison with their macroscopic counterparts. Forces relevant to surface are therefore likely to be substantially larger than the forces associated with volumes. The zeta-potential surface force established between the solid electrode and the surrounding electrolyte induces EDL formation. Within this layer, an excessive amount of free charges exists. When these charges are exposed to an electric field with non-zero component parallel to the surface, they start moving accordingly and can provide a significant pumping force to the electrolyte liquid.

In this study, the electroosmotic flowfields bounded by planar and wavy channel walls are investigated when an uniform potential difference is specified across these channels. Numerical investigation of these types of flowfield needs the solution of velocity vector to enable simulation of the transport of positive and negative ions. Non-uniform distribution of ions in a channel with charged walls results in the formation of Coulomb force which further induces fluid motion. This prompts the importance of solving the transport equations for positive and negative ions along with the Navier-Stokes equations. Thus, the study of electroosmotic flow turns out to be relevant to the analysis of incompressible Navier-Stokes equations and ion transport equations.

https://doi.org/10.4208/cicp.230914.040615a Published online by Cambridge University Press

Microchannel flow has been extensively studied experimentally in the past. One can refer to [4,7–10] for an overview. It would be even suitable for us to carry out numerical simulations of this class of problems because one can better control the involved electrohydrodynamic parameters. Provided that flow convection is no longer negligibly small, simulation of the dynamical system of two classes of equations should address more on the effect of convective flux. This issue is particularly essential near the charged channel walls in the presence of an external electric field as the velocity profile becomes much sharper than the case in the same channel without accumulated charges on the wall. High gradient velocity profile must be accurately resolved while solving the electroosmotic equations. This motivates the present development of a scheme, which is not only stable without use of flux or slope limiter but is also very accurate. A combined compact difference scheme has been derived to approximate the first- and the second-order derivative terms at the same time with a seventh- and sixth-order accuracy, respectively.

This article is organized as follows. In Section 2, conservation equations are derived in Cartesian as well as in curvilinear coordinate systems for the coupled differential system of Navier-Stokes and Poisson-Nernst-Planck equations. Iterative correction of the pressure and velocity solutions while obtaining a divergence-free flow solution is described in Section 3. In Section 4, four problems amenable to exact solutions are sought with an aim to verify the proposed CCD scheme and the segregated incompressible flow solver. The predicted PNP-NS solutions for an electrolyte fluid containing both of the positive and negative ions in the planar and wavy channels are then discussed in Section 5. Finally, conclusions are drawn in Section 6.

2 Governing equations

In this study, the motion of a binary monovalent electrolyte is numerically investigated at the incompressible limiting condition. Under the reaction-free and dilute conditions for the investigated fluid, the electro-diffusion equations for positive and negative ions $n_i(i=+,-)$ are governed by the equation $dn_i/dt+\nabla\cdot\underline{J}=0$. The ion flux vector $\underline{J}$ in this charge conservation equation results from advection, diffusion and electromigration. If the mechanical stress is negligibly small, then the total flux vector is given as

$$\underline{J}=n_i\underline{u}-D_i\bigtriangledown n_i-\mu_i n_i\bigtriangledown\Phi. \tag{2.1}$$

The total flux vector shown above is composed of three different parts. The first contribution to flux vector comes from the convection of charged ions while the remaining two contributions originate from the spatial variation of charged ions and electric potential (Φ). Because of the ineligible electrolyte velocity vector $\underline{u}$ and in the presence of the electric potential Φ, the current electrohydrodynamic (EHD) simulation study is concerned with the electric and hydrodynamic effects.

The salient feature in EHD flow has association with the irrotational electric field intensity $\underline{E}$ (or $\bigtriangledown\times\underline{E}=0$). The dynamic current is usually small and the magnetic induction

https://doi.org/10.4208/cicp.230914.040615a Published online by Cambridge University Press

is negligible. As a result, the appropriate laws employed in the derivation of EHD equations are essentially those of the electrostatics [11]. The Gauss' law $\bigtriangledown\cdot\underline{D}=q$ relates the net charge density q with the electric displacement $\underline{D}$ ($\equiv\epsilon_0\,\underline{E}$), where $\epsilon_0=8.85\times10^{-12}C/mV$. The charge conservation equation brings in current density in the dynamic equation. Given the flux vector $\underline{J}$, the temporal variation of the diffused negative and positive charge densities in isothermal condition can be modeled by the well known Nernst-Planck (N-P) equations as given below.

$$\frac{\partial n_+}{\partial t}+\underline{u}\cdot\nabla n_+=\nabla\cdot(D_+\nabla n_++\mu_+n_+\nabla\Phi), \tag{2.2}$$

$$\frac{\partial n_-}{\partial t}+\underline{u}\cdot\nabla n_-=\nabla\cdot(D_-\nabla n_--\mu_-n_-\nabla\Phi). \tag{2.3}$$

In the above binary charge conservation equations, the unknown variables n_+ and n_- represent the positive and negative charge densities, respectively. The diffusivity constants D_+ and D_- and the mobilities μ_+ and μ_- are linked with each other by the Einsteiń relation. In this study, the ion (or charge) diffusivities D_+ and D_- are assumed to be equal and are denoted as $D_+=D_-=D$. Mobilities μ_+ and μ_- are modeled as $\mu_+=z_+e/(k_bT)$ and $\mu_-=z_-e/(k_bT)$. For the investigated symmetric electrolyte, the valences z_+ and z_- of ions are assumed to be equal to z. The notations e, k_b and T denote the elementary charge, Boltzmann constant and the absolute temperature, respectively.

In N-P equations (2.2) and (2.3), the charge densities $n_\pm$ should be solved together with the hydrodynamic equations because of the presence of electroosmotic flow velocity $\underline{u}$ in the Eqs. (2.2) and (2.3). In other words, simulation of ion transport problem under consideration involves solving the coupled hydrodynamic and electric field equations. It is also worthy to note that Eqs. (2.2-2.3) are derived without taking into account the dissociation and recombination of positive/negative charges.

One can decompose the electric potential Φ into two components [12]. The first potential ϕ is due to an externally applied electric field and the second potential ψ results from the charges attached to channel walls, thereby leading to $\Phi=\phi+\psi$. Eqs. (2.2-2.3) can be therefore rewritten as

$$\frac{\partial n_+}{\partial t}+\underline{u}\cdot\nabla n_+=\nabla\cdot\left[D_+\nabla n_++\frac{ze}{k_bT}n_+\nabla(\phi+\psi)\right], \tag{2.4}$$

$$\frac{\partial n_-}{\partial t}+\underline{u}\cdot\nabla n_-=\nabla\cdot\left[D_-\nabla n_--\frac{ze}{k_bT}n_-\nabla(\phi+\psi)\right]. \tag{2.5}$$

In the presence of the electromigration terms $n_+\nabla\Phi$ and $n_-\nabla\Phi$, calculation of the solutions n_+ and n_- from the above differential system of N-P equations should be coupled with the electric field equation. For the sake of closure, the equations governing the EDL potential ψ and the potential ϕ resulting from the applied electric field $\underline{E}$ must be derived.

The electric potential Φ is governed by the relation $\bigtriangledown^2\Phi=-\rho_e/\epsilon$ or $\bigtriangledown^2\phi+\bigtriangledown^2\psi=-\rho_e/\epsilon$, where ϵ denotes the electrical permittivity of the electrolyte. The potential ϕ in

https://doi.org/10.4208/cicp.230914.040615a Published online by Cambridge University Press

the current simulation study is thus governed by the following Laplace equation in the context of electrostatics

$$\bigtriangledown^2\phi=0. \tag{2.6}$$

As for the electric double layer potential ψ, it is modeled by the Poisson equation given below

$$\bigtriangledown^2\psi=-\frac{\rho_e}{\epsilon_r\epsilon_0}=-\frac{\rho_e}{\epsilon}. \tag{2.7}$$

In the above, $\rho_e\equiv\Sigma_i e\ z_i n_i$ denotes the volume charge density and ϵ_r and ϵ_0 are the dielectric constants of the solution and vacuum, respectively. For a symmetric electrolyte solution, the Poisson equation given above can be further approximated as

$$\bigtriangledown^2\psi=-\frac{ze(n_+-n_-)}{\epsilon_r\epsilon_0}. \tag{2.8}$$

In summary, the Nernst-Planck equations governing the temporal variation of binary charge densities and the Poisson equation modeling the electrostatic potential constitute a PNP system of differential equations.

The electrolyte velocity present in the PNP Eqs. (2.4), (2.5), (2.6), (2.8) led us to take the hydrodynamic equations into consideration. Due to the coupling of electric and hydrodynamic field equations, the Lorentz force (or Coulomb force) vector $\rho_e\underline{E}$ should be also accounted in the numerical simulation of dielectric fluid flow. Substituting the electric charge density $\rho_e=ze(n_+-n_-)$ and the electric field density $\underline{E}\equiv-\nabla\Phi$ into the Lorentz force expression, the force vector $\rho_e\underline{E}$ turns out to be $-ze\ (n_+-n_-)\nabla\Phi$. The resulting momentum vector equation for the fluid flow investigated under the incompressible condition takes the following form

$$\frac{\partial\underline{u}}{\partial t}+\underline{u}\cdot\nabla\underline{u}=-\frac{1}{\rho}\nabla p+\nu\nabla^2\underline{u}+\frac{ze(n_--n_+)}{\rho}\nabla(\psi+\phi). \tag{2.9}$$

Electric potential is governed by $\rho_e=-\epsilon\nabla^2\Phi$ [12]. As a result, the Lorentz force can be represented by $\rho_e\underline{E}=\epsilon\nabla^2\Phi\cdot\nabla\Phi$. In other words, Eq. (2.9) can be represented differently in terms of the electric potential Φ given below

$$\frac{\partial\underline{u}}{\partial t}+\underline{u}\cdot\nabla\underline{u}=-\frac{1}{\rho}\nabla p+\nu\nabla^2\underline{u}+\frac{\epsilon}{\rho}\bigtriangledown^2\Phi\cdot\nabla\Phi. \tag{2.10}$$

The above nonlinear equation will be solved subject to the following divergence-free mathematical constraint condition for $\underline{u}$ (physical mass conservation equation)

$$\nabla\cdot\underline{u}=0. \tag{2.11}$$

In the above, ρ, p and ν denote the fluid density, pressure and fluid viscosity, respectively. The prescribed boundary conditions are detailed in the result section.

https://doi.org/10.4208/cicp.230914.040615a Published online by Cambridge University Press

For generality purposes, all the dependent and independent variables shown in the dimensional PNP equations are normalized according to the definitions given by $x^*=\frac{x}{h}$, $y^*=\frac{y}{h}$, $t^*=\frac{tU_0}{h}$, $u^*=\frac{u}{U_0}$, $v^*=\frac{v}{U_0}$, $p^*=\frac{\triangle p}{\rho U_0^2}$, $\psi^*=\frac{ze}{k_bT}\psi$, $n_\pm^*=\frac{n_\pm}{n_0}$, $\phi^*=\frac{ze}{k_bT}\phi$, $K=\frac{1}{\lambda_D}=(\frac{2n_0z^2e^2}{\epsilon_r\epsilon_0k_bT})^{\frac{1}{2}}$ and $U_0=-\frac{\epsilon_r\epsilon_0\zeta_0Ex}{\mu}$, where ϵ_0 is the permittivity of vacuum, n_0 the bulk concentration, and ζ_0 the surface zeta potential. The derived dimensionless NS equations are summarized below

$$\bigtriangledown^*\cdot\underline{u}^*=0, \tag{2.12}$$

$$\frac{\partial\underline{u}^*}{\partial t^*}+(\underline{u}^*\cdot\bigtriangledown^*)\underline{u}^*=-\bigtriangledown^*p^*+\frac{1}{Re}\bigtriangledown^{*2}\underline{u}^*+\frac{n_0e\zeta_0}{\rho U_0^2}(n_-^*-n_+^*)\bigtriangledown^*(\psi^*+\phi^*). \tag{2.13}$$

As for the normalized PNP equations, they are reformulated as

$$\bigtriangledown^{*2}\psi^*=-\frac{h^2}{2\lambda_D^2}(n_+^*-n_-^*), \tag{2.14}$$

$$\bigtriangledown^{*2}\phi^*=0, \tag{2.15}$$

$$\frac{\partial n_+^*}{\partial t^*}+\bigtriangledown^*\cdot\left[\underline{u}^*n_+^*-\frac{1}{ScRe}\bigtriangledown^*n_+^*-\frac{1}{ScRe}n_+^*\bigtriangledown^*(\psi^*+\phi^*)\right]=0, \tag{2.16}$$

$$\frac{\partial n_-^*}{\partial t^*}+\bigtriangledown^*\cdot\left[\underline{u}^*n_-^*-\frac{1}{ScRe}\bigtriangledown^*n_-^*+\frac{1}{ScRe}n_-^*\bigtriangledown^*(\psi^*+\phi^*)\right]=0. \tag{2.17}$$

In the above, Re $(\equiv\rho hU_0/\mu)$ and Sc $(\equiv\mu/(\rho D))$ denote the Reynolds and Schmidt numbers, respectively.

While solving the differential set of Eqs. (2.12)-(2.17) in an irregular physical domain, one can transform these equations derived in Cartesian coordinates (x,y) to the curvilinear coordinates (ξ,η) through a one-to-one mapping. After performing the transformation of equations between two coordinate systems, Eqs. (2.12)-(2.17) are transformed in curvilinear coordinates (ξ,η) as shown in the following set of dimensionless equations

$$\xi_x\frac{\partial u}{\partial\xi}+\eta_x\frac{\partial u}{\partial\eta}+\xi_y\frac{\partial v}{\partial\xi}+\eta_y\frac{\partial v}{\partial\eta}=0, \tag{2.18}$$

$$\frac{\partial\underline{u}}{\partial t}+U\frac{\partial\underline{u}}{\partial\xi}+V\frac{\partial\underline{u}}{\partial\eta}=-\bigtriangledown p+\frac{1}{Re}\bigtriangledown^2\underline{u}+\frac{n_0e\zeta_0}{\rho U_0^2}(n_--n_+)\bigtriangledown(\psi+\phi), \tag{2.19}$$

$$\begin{aligned}J\left(\alpha\frac{\partial^2\psi}{\partial\xi^2}-2\beta\frac{\partial^2\psi}{\partial\xi\partial\eta}+\gamma\frac{\partial^2\psi}{\partial\eta^2}\right)+\left[\left(\alpha\frac{\partial^2x}{\partial\xi^2}-2\beta\frac{\partial^2x}{\partial\xi\partial\eta}+\gamma\frac{\partial^2x}{\partial\eta^2}\right)\left(y_\xi\frac{\partial\psi}{\partial\eta}-y_\eta\frac{\partial\psi}{\partial\xi}\right)\right.\\ \left.+\left(\alpha\frac{\partial^2y}{\partial\xi^2}-2\beta\frac{\partial^2y}{\partial\xi\partial\eta}+\gamma\frac{\partial^2y}{\partial\eta^2}\right)\left(x_\eta\frac{\partial\psi}{\partial\xi}-x_\xi\frac{\partial\psi}{\partial\eta}\right)\right]=-\frac{h^2J^3}{2\lambda_D^2}(n_+-n_-),\end{aligned} \tag{2.20}$$

$$\begin{aligned}J\left(\alpha\frac{\partial^2\phi}{\partial\xi^2}-2\beta\frac{\partial^2\phi}{\partial\xi\partial\eta}+\gamma\frac{\partial^2\phi}{\partial\eta^2}\right)+\left[\left(\alpha\frac{\partial^2x}{\partial\xi^2}-2\beta\frac{\partial^2x}{\partial\xi\partial\eta}+\gamma\frac{\partial^2x}{\partial\eta^2}\right)\left(y_\xi\frac{\partial\phi}{\partial\eta}-y_\eta\frac{\partial\phi}{\partial\xi}\right)\right.\\ \left.+\left(\alpha\frac{\partial^2y}{\partial\xi^2}-2\beta\frac{\partial^2y}{\partial\xi\partial\eta}+\gamma\frac{\partial^2y}{\partial\eta^2}\right)\left(x_\eta\frac{\partial\phi}{\partial\xi}-x_\xi\frac{\partial\phi}{\partial\eta}\right)\right]=0,\end{aligned} \tag{2.21}$$

https://doi.org/10.4208/cicp.230914.040615a Published online by Cambridge University Press

$$\frac{\partial n_+}{\partial t}+U\frac{\partial n_+}{\partial \xi}+V\frac{\partial n_+}{\partial \eta}=\frac{1}{ScRe}\nabla^2 n_+ +\frac{1}{ScRe}n_+\nabla^2(\psi+\phi)$$
$$+\frac{1}{ScRe}\left[\left(\xi_x\frac{\partial n_+}{\partial \xi}+\eta_x\frac{\partial n_+}{\partial \eta}\right)\left(\xi_x\frac{\partial \psi}{\partial \xi}+\eta_x\frac{\partial \psi}{\partial \eta}+\xi_x\frac{\partial \phi}{\partial \xi}+\eta_x\frac{\partial \phi}{\partial \eta}\right)\right.$$
$$\left.+\left(\xi_y\frac{\partial n_+}{\partial \xi}+\eta_y\frac{\partial n_+}{\partial \eta}\right)\left(\xi_y\frac{\partial \psi}{\partial \xi}+\eta_y\frac{\partial \psi}{\partial \eta}+\xi_y\frac{\partial \phi}{\partial \xi}+\eta_y\frac{\partial \phi}{\partial \eta}\right)\right], \quad (2.22)$$

$$\frac{\partial n_-}{\partial t}+U\frac{\partial n_-}{\partial \xi}+V\frac{\partial n_-}{\partial \eta}=\frac{1}{ScRe}\nabla^2 n_- -\frac{1}{ScRe}n_-\nabla^2(\psi+\phi)$$
$$-\frac{1}{ScRe}\left[\left(\xi_x\frac{\partial n_-}{\partial \xi}+\eta_x\frac{\partial n_-}{\partial \eta}\right)\left(\xi_x\frac{\partial \psi}{\partial \xi}+\eta_x\frac{\partial \psi}{\partial \eta}+\xi_x\frac{\partial \phi}{\partial \xi}+\eta_x\frac{\partial \phi}{\partial \eta}\right)\right.$$
$$\left.+\left(\xi_y\frac{\partial n_-}{\partial \xi}+\eta_y\frac{\partial n_-}{\partial \eta}\right)\left(\xi_y\frac{\partial \psi}{\partial \xi}+\eta_y\frac{\partial \psi}{\partial \eta}+\xi_y\frac{\partial \phi}{\partial \xi}+\eta_y\frac{\partial \phi}{\partial \eta}\right)\right]. \quad (2.23)$$

In the above, $U(\equiv u\xi_x+v\xi_y)$ and $V(\equiv u\eta_x+v\eta_y)$ are denoted as the contravariant velocity components, respectively, and $\alpha=x_\eta^2+y_\eta^2$, $\beta=x_\xi x_\eta+y_\xi y_\eta$, $\gamma=x_\xi^2+y_\xi^2$, $J=x_\xi y_\eta-x_\eta y_\xi$.

3 Numerical method

After approximating the time derivative term ϕ_t using the Euler time-stepping scheme for the model equation $\phi_t+a\phi_x+b\phi_y+c\phi=k\nabla^2\phi+f$, the semi-discretized equation for $\overline{\phi}(\equiv\overline{\phi}^{n+1})$ is derived as follows

$$\bar{a}\,\frac{\partial\overline{\phi}}{\partial x}+\bar{b}\,\frac{\partial\overline{\phi}}{\partial y}+\bar{c}\,\overline{\phi}-\bar{k}\,\left(\frac{\partial^2\overline{\phi}}{\partial x^2}+\frac{\partial^2\overline{\phi}}{\partial y^2}\right)=\bar{f}, \quad (3.1)$$

where $\bar{a}=a\triangle t$, $\bar{b}=b\triangle t$,$\bar{c}=c\triangle t+1$, $\bar{k}=k\triangle t$, $\bar{f}=f\triangle t+\phi^n$. To describe the numerical method developed for the approximation of the spatial derivative terms shown above, the model transport equation for $\overline{\phi}$ has been approximated at a constant diffusion coefficient $\bar{k}$. The two coefficients $\bar{a}$ and $\bar{b}$ in (3.1) are denoted as the constant velocities along the respective x- and y-direction, and $\bar{f}$ is a source term.

3.1 Combined compact difference scheme for spatial derivative terms

The first-order derivative term $\partial\overline{\phi}/\partial x$ and the second-order derivative term $\partial^2\overline{\phi}/\partial x^2$ in Eq. (3.1) will be approximated in a mesh of constant grid spacing $\Delta x=\Delta y=h$. In the finite difference context, our strategy of approximating these spatial derivative terms in Eq. (3.1) underlies the following five-point upwinding combined compact difference scheme

$$a_1\frac{\partial\overline{\phi}}{\partial x}|_{i-1}+\frac{\partial\overline{\phi}}{\partial x}|_i+a_3\frac{\partial\overline{\phi}}{\partial x}|_{i+1}$$
$$=-h\left(b_1\frac{\partial^2\overline{\phi}}{\partial x^2}|_{i-1}+b_2\frac{\partial^2\overline{\phi}}{\partial x^2}|_i+b_3\frac{\partial^2\overline{\phi}}{\partial x^2}|_{i+1}\right)+\frac{1}{h}\left(c_1\overline{\phi}_{i-2}+c_2\overline{\phi}_{i-1}+c_3\overline{\phi}_i+c_4\overline{\phi}_{i+1}\right), \quad (3.2)$$

https://doi.org/10.4208/cicp.230914.040615a Published online by Cambridge University Press

$$\overline{b}_1\frac{\partial^2\overline{\phi}}{\partial x^2}|_{i-1}+\frac{\partial^2\overline{\phi}}{\partial x^2}|_i+\overline{b}_3\frac{\partial^2\overline{\phi}}{\partial x^2}|_{i+1}$$
$$=\frac{1}{h^2}\left(\overline{c}_1\overline{\phi}_{i-1}+\overline{c}_2\overline{\phi}_i+\overline{c}_3\overline{\phi}_{i+1}\right)-\frac{1}{h}\left(\overline{a}_1\frac{\partial\overline{\phi}}{\partial x}|_{i-1}+\overline{a}_2\frac{\partial\overline{\phi}}{\partial x}|_i+\overline{a}_3\frac{\partial\overline{\phi}}{\partial x}|_{i+1}\right). \tag{3.3}$$

Similarly, one can approximate the other two terms $\frac{\partial\overline{\phi}}{\partial y}$ and $\frac{\partial^2\overline{\phi}}{\partial y^2}$ along the y-direction. Approximations of the derivative terms $\frac{\partial\overline{\phi}}{\partial x}|_i$ and $\frac{\partial^2\overline{\phi}}{\partial x^2}|_i$ are coupled through the terms $\frac{\partial\overline{\phi}}{\partial x}|_{i-1}$, $\frac{\partial\overline{\phi}}{\partial x}|_i$, $\frac{\partial\overline{\phi}}{\partial x}|_{i+1}$, $\frac{\partial^2\overline{\phi}}{\partial x^2}|_{i-1}$, $\frac{\partial^2\overline{\phi}}{\partial x^2}|_i$, $\frac{\partial^2\overline{\phi}}{\partial x^2}|_{i+1}$, $\overline{\phi}_{i-2}$, $\overline{\phi}_{i-1}$, $\overline{\phi}_i$ and $\overline{\phi}_{i+1}$. For simplicity purposes, the above coefficients will be determined for the case with a positive-valued convective coefficient. For the case of a negative-valued convective coefficient, the derivation remains the same.

The second-order derivative terms are normally approximated by centered schemes. As a result, the weighting coefficients shown in Eq. (3.2) can be determined solely from the modified equation analysis for getting a physically correct approximation. Coefficients $\overline{a}_1, \overline{a}_2, \overline{a}_3, \overline{b}_1, \overline{b}_3, \overline{c}_1, \overline{c}_2$ and $\overline{c}_3$ in (3.3) are derived as follows. Taylor series expansions are used to expand the terms $\overline{\phi}_{i\pm1}$, $\frac{\partial\overline{\phi}}{\partial x}|_{i\pm1}$ and $\frac{\partial^2\overline{\phi}}{\partial x^2}|_{i\pm1}$ with respect to $\overline{\phi}_i$, $\frac{\partial\overline{\phi}}{\partial x}|_i$ and $\frac{\partial^2\overline{\phi}}{\partial x^2}|_i$. The leading eight error terms in the modified equations are then eliminated to get the same number of algebraic equations for Eq. (3.3). The coefficients shown in Eq. (3.3) are then derived as $\overline{a}_1=-\frac{9}{8}$, $\overline{a}_2=0$, $\overline{a}_3=\frac{9}{8}$, $\overline{b}_1=-\frac{1}{8}$, $\overline{b}_3=-\frac{1}{8}$, $\overline{c}_1=3$, $\overline{c}_2=-6$, $\overline{c}_3=3$. The resulting modified equation for $\frac{\partial^2\overline{\phi}}{\partial x^2}$ has the spatial accuracy of order six [13].

There are total nine unknown coefficients in Eq. (3.2). These coefficients are obtained using the modified equation analysis approach of [13]. Taylor series expansions for the terms ϕ_{i-2}, $\phi_{i\pm1}$, $\frac{\partial\phi}{\partial x}|_{i\pm1}$ and $\frac{\partial^2\phi}{\partial x^2}|_{i\pm1}$ are performed with respect to ϕ_i, $\frac{\partial\phi}{\partial x}|_i$ and $\frac{\partial^2\phi}{\partial x^2}|_i$ to obtain the following eight algebraic equations

$$\begin{aligned}
&c_1+c_2+c_3+c_4=0,\\
&-2c_1-c_2+c_4-a_1-a_3=1,\\
&2c_1+\frac{1}{2}(c_2+c_4)+a_1-a_3-b_1-b_2-b_3=0,\\
&\frac{-4}{3}c_1+\frac{1}{6}(c_4-c_2)-\frac{1}{2}(a_1+a_3)+b_1-b_3=0,\\
&\frac{2}{3}c_1+\frac{1}{24}(c_4+c_2)+\frac{1}{6}(a_1-a_3)-\frac{1}{2}(b_1+b_3)=0,\\
&\frac{-4}{15}c_1+\frac{1}{120}(c_4-c_2)-\frac{1}{24}(a_1+a_3)+\frac{1}{6}(b_1-b_3)=0,\\
&\frac{4}{45}c_1+\frac{1}{720}(c_4+c_2)+\frac{1}{120}(a_1-a_3)-\frac{1}{24}(b_1+b_3)=0,\\
&\frac{-8}{315}c_1+\frac{1}{5040}(c_4-c_2)-\frac{1}{720}(a_1+a_3)+\frac{1}{120}(b_1-b_3)=0.
\end{aligned}$$

In order to uniquely determine all nine unknown coefficients, we need an additional equation. For a more accurate approximation of the first-order derivative term in Eq. (3.2),

https://doi.org/10.4208/cicp.230914.040615a Published online by Cambridge University Press

the exact dispersion relation for $\partial\phi/\partial x$ serves as our guideline. This results in a better linkage between the angular frequency and numerical wavenumber [13, 14]. If the numerical dispersion relation is close to its exact counterpart, the solution can then be accurately predicted. Thus the developed scheme must accommodate the dispersion relation preserving nature for the first-order derivative term.

Fourier transform and its inverse of ϕ are given respectively as $\tilde{\phi}(\alpha)=1/(2\pi)\times\int_{-\infty}^{+\infty}\phi(x)\exp(-\mathbf{i}\alpha x)\,dx$ and $\phi(x)=\int_{-\infty}^{+\infty}\tilde{\phi}(\alpha)\,\exp(\mathbf{i}\alpha x)\,d\alpha$ [13]. Fourier transform on each term shown in Eqs. (3.2) and (3.3) has been performed to get the relation between the exact wavenumber α and the numerical wavenumber α'. For getting a more accurate phase computation, it is rational to equate the equations for α' and α'' to their exact ones in the first and second order derivative terms [13, 14],

$$\begin{aligned}&\mathbf{i}\alpha' h\big(a_1\exp(-\mathbf{i}\alpha h)+1+a_3\exp(\mathbf{i}\alpha h)\big)\\&=-(\mathbf{i}\alpha'' h)^2\big(b_1\exp(-\mathbf{i}\alpha h)+b_2+b_3\exp(\mathbf{i}\alpha h)\big)+c_1\exp(-2\mathbf{i}\alpha h)+c_2\exp(-\mathbf{i}\alpha h)\\&\quad+c_3+c_4\exp(\mathbf{i}\alpha h),\end{aligned}\tag{3.4}$$

$$\begin{aligned}&\mathbf{i}\alpha' h\left(-\frac{9}{8}\exp(-\mathbf{i}\alpha h)+\frac{9}{8}\exp(\mathbf{i}\alpha h)\right)\\&=-(\mathbf{i}\alpha'' h)^2\left(-\frac{1}{8}\exp(-\mathbf{i}\alpha h)+1-\frac{1}{8}\exp(\mathbf{i}\alpha h)\right)+3\exp(-\mathbf{i}\alpha h)-6+3\exp(\mathbf{i}\alpha h).\end{aligned}\tag{3.5}$$

Expression for α' is derived by solving Eqs. (3.4) and (3.5).

For acquiring the derived dispersion relation preserving nature, the exact (αh) and the numerical $(\alpha' h)$ wavenumber must match with each other. Thus, one can define an error function $E(\alpha)$ as given below.

$$E(\alpha)=\int_0^{\frac{7\pi}{8}}\big[(\alpha h-\Re[\alpha' h])\big]^2 d(\alpha h)=\int_0^{\frac{7\pi}{8}}\big[(\gamma-\Re[\gamma'])\big]^2 d\gamma,\tag{3.6}$$

where $\gamma=\alpha h$ and $\gamma'=\alpha' h$. In this expression $\Re[\alpha' h]$ denotes the real part of $\alpha' h$. A condition $\partial E/\partial c_3=0$ is applied to minimize E. This constraint equation along with the other eight previously derived algebraic equations uniquely determine nine introduced unknowns as,

$$\begin{aligned}&a_1=1.8348198717722105327, && a_3=-0.89037542732776608826,\\&b_1=0.25771089743383732115, && b_2=-1.0925307692060478538,\\&b_3=0.091044230767170654483, && c_1=1/54, \quad c_2=-4.4967487178827942769,\\&c_3=6.9934974357655885538, && c_4=-2.5152672364013127954.\end{aligned}$$

The derived upwinding combined compact difference scheme for $\partial\phi/\partial x$ has the spatial accuracy of order seven.

Unlike the purely upwinding CCD scheme developed earlier in [13], two extra stencil points are taken into account in this study to improve scheme performance. For the

https://doi.org/10.4208/cicp.230914.040615a Published online by Cambridge University Press

reference point i, one additional point at the upwind side, namely the $i-2$ nodal point, is considered for the positive-valued velocity case to not only enhance the convective stability but also to improve the accuracy order. In the same vein, the stencil point $i+2$ has been involved for the case with negative valued velocity. The resulting adopted stencil points $i-2$, $i-1$, i, $i+1$ and $i-1$, i, $i+1$, $i+2$ for the positive and negative velocities are exactly the same as those used in the well known QUICK scheme (Quadratic Upstream Interpolation for Convective Kinetics) for the approximation of the first order derivative term in the transport equation [15]. As for the discretization of the second-order derivative term in the currently proposed CCD scheme, physically plausible center scheme is chosen. It is worthy to address here that two additional stencil points have nothing to do with the left hand side of the above CCD equations. The matrix equations for solving the first and second derivative terms remain tri-diagonal and hence does not increase computational cost.

In Fig. 1(a) we have compared the resolving abilities of different schemes for the first derivative. Under our expectation, the newly proposed CCD scheme outperforms the purely upwinding schemes of [13, 15] over the entire modified wavenumber range. Fig. 1 clearly shows the excellent spectral-like accuracy while evaluating the first- and the second-order derivative terms.

Prior to solving complex unsteady flow problems, one needs the information about the combined effects of the spatial and the temporal discretization schemes on the simulation. Thus the numerical analysis should not be only restricted to the estimation of the spectral resolution for the spatial derivative terms. For an accurate simulation, one needs to resolve all the spatial and the temporal scales present in the flow domain. In addition, one needs to ensure that all the resolved components propagate with correct physical velocity as dictated by the physical dispersion relation [16]. Most of the numerical schemes display spurious unphysical behavior for the high wavenumber components which are capable of triggering numerical instabilities. Such unphysical components are needed to be attenuated either by using upwinding schemes or by filtering [16]. In the present work, we have proposed the spectrally optimized upwinding scheme in the same spirit.

For the proposed spatial discretization scheme, important numerical properties such as the numerical amplification factor contours and the normalized numerical group velocity contours are obtained following the work in [16–18] for the solution of 1D wave equation when a four stage fourth order Runge-Kutta $RK4$ scheme has been used for the time discretization. The model 1D wave equation is given by,

$$\frac{\partial u}{\partial t}+c\frac{\partial u}{\partial x}=0, \quad c>0. \tag{3.7}$$

Calibration of numerical schemes for the model 1D wave equation has been advocated in [16] as it has non-dispersive, non-dissipative physical nature while most of solutions from the numerical schemes provide dispersive and dissipative solution. Consider a domain with a discrete grid of uniform grid spacing h. Variable u at the j^{th} node can be represented by its bi-lateral Fourier-Laplace transform as, $u(x_j,t)=\int U(k,t)\,e^{ikx_j}\,dk$,

https://doi.org/10.4208/cicp.230914.040615a Published online by Cambridge University Press

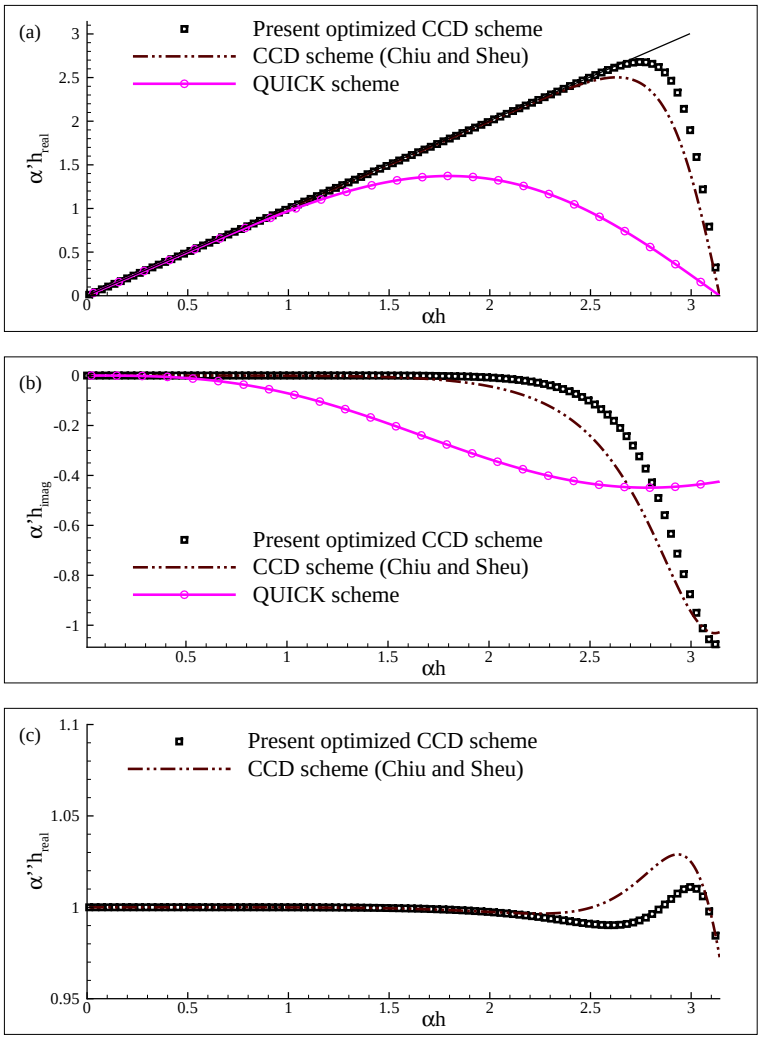


Figure 1: Fourier analysis of errors for the real and imaginary parts of the first and second derivatives, which are shown in (a), (b) and (c), respectively, for the indicated numerical schemes.

where k is a wavenumber. Difference approximations involve truncation of the higher order derivative terms which causes truncation error. The exact and the numerical spatial derivatives can be represented in the spectral plane as [16],

$$\left[\frac{\partial u}{\partial x}\right]_{exact} = \int ikU\, e^{ikx_j}\, dk,$$
$$\left[\frac{\partial u}{\partial x}\right]_{numerical} = \int ik_{eq}U\, e^{ikx_j}\, dk.$$

Any difference scheme (explicit or implicit) can be represented in the matrix form as $[A]u' = [B]u$. Matrix $[A]$ is an identity matrix for explicit schemes while it is either tridiag-

https://doi.org/10.4208/cicp.230914.040615a Published online by Cambridge University Press

onal or pentadigonal for the implicit compact difference schemes. Representations of the difference scheme can be simplified as $u'=[C]u$, where $[C]=[A]^{-1}[B]$ [16]. Assuming the domain has N equi-spaced grid points, the first derivative at the j^{th} node in the matrix form and the spectral form are given as [16,18],

$$u_j^{'}=\frac{1}{h}\sum_{l=1}^{N}C_{jl}\,u_l,$$
$$u_j^{'}=\int\frac{1}{h}\sum C_{jl}\,U\,e^{ik(x_l-x_j)}\,e^{ikx_j}\,dk.$$

Using above expression, for the 1D wave equation (3.7) one can further write,

$$\frac{\Delta U}{U}=-\left[\frac{c\Delta t}{h}\right]\sum_{l=1}^{N}C_{jl}\,e^{ik(x_l-x_j)} \tag{3.8}$$

where the non-dimensional term $(\frac{c\Delta t}{h})$ is identified as the CFL number (N_c). One can define a numerical amplification factor as the ratio of the spectral amplitudes at successive time steps as, $(G_j=U_j(k,t^{(n+1)})/U_j(k,t^{(n)}))$. For the $RK4$ scheme, the numerical amplification factor is given as [16,17],

$$G_j=1-A_j+\frac{A_j^2}{2}-\frac{A_j^3}{6}+\frac{A_j^4}{24} \tag{3.9}$$

where $A_j=N_c\sum_{l=1}^{N}C_{jl}\,e^{ik(x_l-x_j)}$. After evaluating spectral information for the numerical amplification factor, one can write the general solution at any time stage by,

$$u_j^n=\int A_0(k)\,[|G_j|]^n\,e^{i(kx_j-n\beta_j)}\,dk \tag{3.10}$$

where $A_0(k)$ is the initial input spectrum and β_j is given by, $tan^{-1}[-\frac{(G_j)_{imag}}{(G_j)_{real}}]$ that can be related to the numerical phase speed c_N. Authors in [16,17], provided the correct numerical dispersion relation as, $\omega_N=c_Nk$. Using the numerical dispersion relation, general numerical solution of Eq. (3.7) is given as,

$$u_N=\int A_0(k)[|G|]^{t/\Delta t}e^{ik(x-c_Nt)}dk. \tag{3.11}$$

Above expression leads to the normalized numerical phase speed and group velocity at the j^{th} node for Eq. (3.7) are given by [16,17],

$$\left[\frac{c_N}{c}\right]_j=\frac{\beta_j}{\omega\Delta t}, \tag{3.12}$$
$$\left[\frac{V_{gN}}{c}\right]_j=\frac{1}{N_c}\frac{d\beta_j}{d(kh)}. \tag{3.13}$$

https://doi.org/10.4208/cicp.230914.040615a Published online by Cambridge University Press

We have shown the numerical amplification factor $|G_j|$ contours and the normalized numerical group velocity V_{gN}/c contours in Fig. 2(a) and (b), respectively. For numerically stable computations, numerical amplification factor should be less than one. The lower CFL number N_c and lower wavenumber kh region where $|G_j|=1$ property is observed is known as neutrally stable region. Solution components in this region are neither amplified nor attenuated numerically. For stability purpose, one is forced to compute in a lower CFL number zone. However, in addition to the numerical stability, one needs to ensure all the resolved components propagate with correct velocity. Normalized numerical group velocity V_{gN}/c contours in Fig. 2(b) help to identify a region where solution components will propagate with a correct physical speed. For the solution of Eq. (3.7), all the solution components should propagate at phase speed c. Thus one should look for the region in the N_c-kh plane where $V_{gN}/c=1$ property is observed. Computations belonging to this region only guarantee preservation of the physical dispersion relation. For the proposed scheme, one observes preservation of physical dispersion relation up to $kh=2.5$ with 1% error when the computations are performed for small CFL numbers. This is a significant achievement for the proposed DRP scheme as a large band of wavenumber components propagate at correct physical speed.

While solving a non-periodic problem one needs to prescribe additional stencils for the computation of the spatial derivative terms at the boundary and the near-boundary points located at either end of the domain. Often these stencils use information on either side of the domain causing very unstable or very stable behavior at the domain boundaries. Authors in [19] proposed a new boundary and near-boundary stencils which have significantly improved numerical properties as compared to the stencils used in [13]. These boundary and the near-boundary stencils are given as,

$$f_1'=(-1.5f_1+2f_2-0.5f_3)/h, \tag{3.14}$$

$$f_1''=(f_1-2f_2+f_3)/h^2, \tag{3.15}$$

$$f_N'=-(-1.5f_N+2f_{N-1}-0.5f_{N-2})/h, \tag{3.16}$$

$$f_N''=-(f_N-2f_{N-1}+f_{N-2})/h^2, \tag{3.17}$$

$$f_2'=\frac{1}{h}\left[\left(\frac{2\beta_2}{3}-\frac{1}{3}\right)f_1-\left(\frac{8\beta_2}{3}+\frac{1}{2}\right)f_2+\left(4\beta_2+1\right)f_3-\left(\frac{8\beta_2}{3}+\frac{1}{6}\right)f_4+\frac{2\beta_2}{3}f_5\right], \tag{3.18}$$

$$\begin{aligned}f_{N-1}'=\frac{-1}{h}\Bigg[&\left(\frac{2\beta_{N-1}}{3}-\frac{1}{3}\right)f_N-\left(\frac{8\beta_{N-1}}{3}+\frac{1}{2}\right)f_{N-1}+\left(4\beta_{N-1}+1\right)f_{N-2}\\&-\left(\frac{8\beta_{N-1}}{3}+\frac{1}{6}\right)f_{N-3}+\frac{2\beta_{N-1}}{3}f_{N-4}\Bigg],\end{aligned} \tag{3.19}$$

$$f_2''=(f_1-2f_2+f_3)/h^2, \tag{3.20}$$

$$f_{N-1}''=(f_N-2f_{N-1}+f_{N-2})/h^2, \tag{3.21}$$

where $\beta_2=-0.025$ and $\beta_{N-1}=0.09$. These, boundary and the near-boundary stencils provided in [19] display improved numerical properties and are used in the present work while solving non-periodic problems.

https://doi.org/10.4208/cicp.230914.040615a Published online by Cambridge University Press

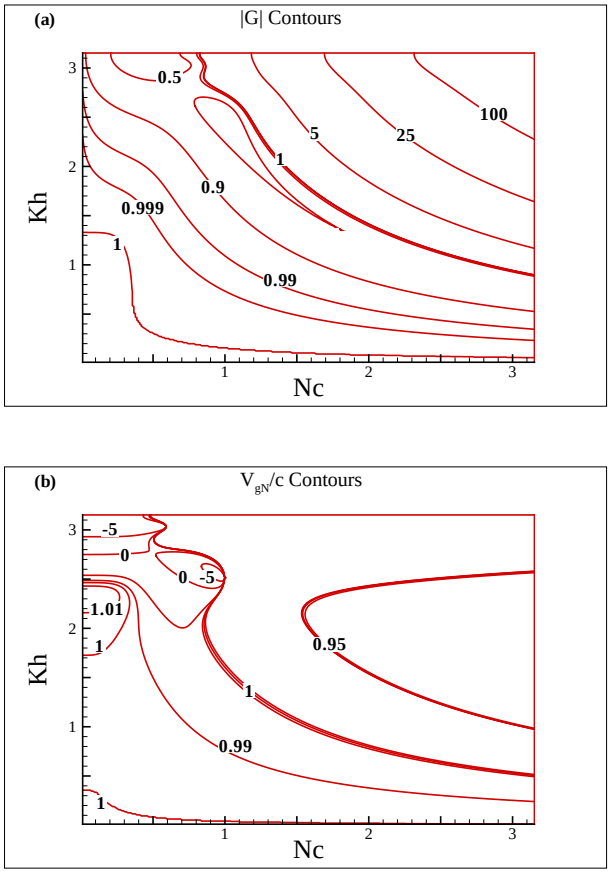


Figure 2: Numerical amplification factor $|G_j|$ contours and the normalized numerical group velocity V_{gN}/c contours are shown in (a) for the solution of 1D wave equation when the spatial discretization is obtained through the spectrally optimized CCD scheme while RK4 for the time integration.

3.2 Incompressible flow solver

Calculation of the electrohydrodynamic equations begins with solving the following two equations in the projection step [20]

$$\frac{\underline{u}^{n+1}-\underline{u}^{n+\frac{1}{2}}}{\Delta t}=-\nabla p^{n+1}, \tag{3.22}$$

$$\nabla\cdot\underline{u}^{n+1}=0. \tag{3.23}$$

Substitution of Eq. (3.22) into the semi-discretized momentum equation leads to

$$\frac{\underline{u}^{n+1}-\underline{u}^{n}}{\Delta t}+\left(\underline{u}^{n+\frac{1}{2}}\cdot\nabla\right)\underline{u}^{n+\frac{1}{2}}-\frac{1}{Re}\nabla^2\underline{u}^{n+\frac{1}{2}}+\nabla p^{n+1}=M_1+M_2+\underline{f}^{n+1}. \tag{3.24}$$

In the above, $M_1=[(\underline{u}^{n+\frac{1}{2}}\cdot\nabla)\nabla p^{n+1}+(\nabla p^{n+1}\cdot\nabla)\underline{u}^{n+\frac{1}{2}}-\frac{1}{Re}\nabla^2(\nabla p^{n+1})]\Delta t$, $M_2=-[(\nabla p^{n+1}\cdot\nabla)\nabla p^{n+1}]\Delta t^2$ and the Coulomb force vector $\underline{f}^{n+1}=\frac{n_0 e\zeta_0}{\rho U_0^2}(n_- - n_+)\bigtriangledown(\psi+\phi)$.

https://doi.org/10.4208/cicp.230914.040615a Published online by Cambridge University Press

Let $p^{n+1}=p^*+p'$, the equation used in the pressure-gradient step is decomposed into the equations $(\underline{u}^*-\underline{u}^{n+\frac{1}{2}})/\Delta t=-\nabla p^*$ and $(\underline{u}^{n+1}-\underline{u}^*)/\Delta t=-\nabla p'$, where p^* is an intermediate pressure [20]. Then, Eq. (3.24) is reformulated as

$$\frac{\underline{u}^{n+1}-\underline{u}^n}{\Delta t}+(\underline{u}^*\cdot\nabla)\underline{u}^*-\frac{1}{Re}\nabla^2\underline{u}^*+\nabla p^*=-\nabla p'+M_3+M_4+\underline{f}^{n+1}, \tag{3.25}$$

where $M_3=[(\underline{u}^*\cdot\nabla)\nabla p'+(\nabla p'\cdot\nabla)\underline{u}^*]\Delta t-\frac{1}{Re}\nabla(\nabla\cdot\underline{u}^*)\Delta t$ and $M_4=-[(\nabla p'\cdot\nabla)\nabla p']\Delta t^2$.

In order to reduce the computational cost, the following algorithm is employed [20]. Given the solutions for the velocity $\underline{u}_1^*$, pressure p_0^*, and $p_0^{'}$.

For $s=1,2,\cdots$

$$\frac{\underline{u}_s^{n+1}-\underline{u}^n}{\Delta t}+\underline{u}_s^*\cdot\nabla\underline{u}_s^*-\frac{1}{Re}\nabla^2\underline{u}_s^*+\nabla p_{s-1}^*=-\nabla p_{s-1}^{'}+M_3+M_4+\underline{f}^{n+1}, \tag{3.26}$$

$$p_s^*=p_{s-1}^*+p_s', \tag{3.27}$$

$$\underline{u}_{s+1}^*=\underline{u}_s^{n+1}-\Delta t\nabla p_s'. \tag{3.28}$$

By performing the divergence operator on the equation $(\underline{u}^{n+1}-\underline{u}^*)/\Delta t=-\nabla p'$, we can get $\nabla\cdot\underline{u}^{n+1}=\nabla\cdot\underline{u}^*-\Delta t\nabla^2 p'$. The divergence-free condition $\nabla\cdot\underline{u}^{n+1}=0$ is enforced to yield the pressure correction equation $\nabla^2 p'=\nabla\cdot\underline{u}^*/\Delta t$. At each interior point (i,j), the centered difference approximation given below for $\nabla^2 p'=\nabla\cdot\underline{u}^*/\Delta t$ is [20]

$$2\left(\frac{1}{\Delta x^2}+\frac{1}{\Delta y^2}\right)p_{i,j}'=-\frac{\nabla\cdot\underline{u}_{i,j}^*}{\Delta t}+\frac{1}{\Delta x^2}(p_{i-1,j}'+p_{i+1,j}')+\frac{1}{\Delta y^2}(p_{i,j-1}'+p_{i,j+1}'). \tag{3.29}$$

Note that the term $(1/\Delta x^2)(p_{i-1,j}'+p_{i+1,j}')+(1/\Delta y^2)(p_{i,j-1}'+p_{i,j+1}')$ is omitted so as to obtain the following equation

$$p_{i,j}'=-\frac{\Delta x^2\Delta y^2}{2(\Delta x^2+\Delta y^2)\Delta t}\nabla\cdot\underline{u}_{i,j}^*. \tag{3.30}$$

Use of the above derived expression for the pressure correction term over-estimates the predicted pressure due to the term being omitted. For the compensation of the term associated with the previously mentioned omission term, Eq. (3.30) is used first to get the following pressure correction term p'^*

$$p_{i,j}'^*=-\frac{\Delta x^2\Delta y^2}{2(\Delta x^2+\Delta y^2)\Delta t}\nabla\cdot\underline{u}_{i,j}^*. \tag{3.31}$$

This is followed by calculating the pressure correction from the value of p'^* according to

$$p_{i,j}'=p_{i,j}'^*+\frac{\Delta y^2}{2(\Delta x^2+\Delta y^2)}(p_{i-1,j}'^*+p_{i+1,j}'^*)+\frac{\Delta x^2}{2(\Delta x^2+\Delta y^2)}(p_{i,j-1}'^*+p_{i,j+1}'^*). \tag{3.32}$$

https://doi.org/10.4208/cicp.230914.040615a Published online by Cambridge University Press

3.3 Algorithm

Before proceeding to the discussion of numerical results for the solution of coupled Navier-Stokes and PNP equations, we provide here an algorithm for solving these equations in a coupled manner. For the solution of electroosmotic flow, one needs to solve Eq. (2.18) to Eq. (2.23) at every time step. All the spatial derivatives involved in these equations are obtained using the proposed spectrally optimized CCD scheme. For a constant electric field, potential ϕ does not vary with time and its effects are directly accounted in Eqs. (2.19), (2.20), (2.22) and (2.23). We have followed the following algorithm while solving the coupled PNP-NS equations.

1. For a given externally applied electric field, solve Eq. (2.20) iteratively to obtain potential ψ resulting from the charges attached to channel walls till the desired convergence is achieved.
2. Solve transport equations for the positive and negative charge densities as given by Eqs. (2.22) and (2.23), respectively using explicit Euler time marching technique.
3. Solution of the Navier-Stokes equations Eq. (2.18) and Eq. (2.19) should be obtained satisfying the incompressibility constraint as explained in Section 3.2.
4. Repeat the steps (1)-(3) till the steady state is achieved.

4 Verification studies

Here, the performance of the newly developed high resolution upwinding CCD scheme applied for solving electroosmotic flow equations has been studied. For this purpose, four different special cases in which the Navier-Stokes equations amenable to analytical solution are considered. We have compared the numerical and the exact solutions for three simplified PNP equations, which are derived under different assumptions, in Sections 4.1-4.4.

4.1 Analytical problem

We have considered a square domain $0 \leq x,y \leq 1$ for obtaining the solution from Navier-Stokes equations without considering the Coulomb force term. It is assumed that the exact solutions for the velocity vector and the scalar pressure take the forms of $u(x,y) = \frac{-2(1+y)}{(1+x)^2+(1+y)^2}$, $v(x,y) = \frac{2(1+x)}{(1+x)^2+(1+y)^2}$ and $p(x,y) = \frac{-2}{(1+x)^2+(1+y)^2}$ provided that the source terms are derived accordingly by substituting the exact solutions into their respective Eq. (2.12) and Eq. (2.13). In addition, the exact solutions for n_+, n_-, ψ, ϕ are also assumed to take the following forms provided that the source terms are derived by substituting

https://doi.org/10.4208/cicp.230914.040615a Published online by Cambridge University Press

Table 1: The computed L_2 error norms in six uniform grids for the Navier-Stokes equations.

Grid	10^2	20^2	30^2	40^2	50^2	60^2
u	1.77×10^{-4}	5.70×10^{-5}	2.65×10^{-5}	1.52×10^{-5}	9.82×10^{-6}	6.83×10^{-6}
v	2.12×10^{-4}	5.60×10^{-5}	2.54×10^{-5}	1.44×10^{-5}	9.32×10^{-6}	6.50×10^{-6}
p	7.45×10^{-3}	2.02×10^{-3}	1.02×10^{-3}	6.39×10^{-4}	4.44×10^{-4}	3.30×10^{-4}

Table 2: The computed L_2 error norms in six uniform grids for $n_\pm$, ψ and ϕ in the Poisson-Nernst-Planck equations.

Grid	10^2	20^2	30^2	40^2	50^2	60^2
n_+	7.03×10^{-4}	2.00×10^{-4}	9.32×10^{-5}	5.35×10^{-5}	3.46×10^{-5}	2.41×10^{-5}
n_-	1.50×10^{-4}	4.41×10^{-5}	2.11×10^{-5}	1.27×10^{-5}	8.85×10^{-6}	6.75×10^{-6}
ψ	1.06×10^{-5}	2.76×10^{-6}	1.20×10^{-6}	6.49×10^{-7}	3.94×10^{-7}	2.58×10^{-7}
ϕ	3.60×10^{-5}	9.49×10^{-6}	4.29×10^{-6}	2.44×10^{-6}	1.57×10^{-6}	1.10×10^{-6}

the exact solutions for u, v, p into their respective Eqs. (2.14)-(2.17)

$$n_+(x,y)=\frac{-2(1+y)}{(1+x)^2+(1+y)^2}, \tag{4.1}$$

$$n_-(x,y)=\frac{-2(1+y)}{(1+x)^2+(1+y)^2}, \tag{4.2}$$

$$\psi(x,y)=\frac{-2}{(1+x)^2+(1+y)^2}, \tag{4.3}$$

$$\phi(x,y)=\frac{-2}{(1+x)^2+(1+y)^2}. \tag{4.4}$$

Calculations were performed on the different equi-spaced meshes with grid spacings $1/10, 1/20, 1/30, 1/40, 1/50, 1/60$. For these calculations, time step of $\Delta t=10^{-6}$ has been used. The predicted L_2 *error norms* are tabulated in Tables 1 and 2. The resulting spatial rates of convergence are shown in Figs. 3 and 4. Solution obtained on the coarsest grid with a grid spacing of $1/10$ has the maximum error of the order of 10^{-3} which can be reduced further as we reduce the grid spacing. Thus, the proposed upwinding combined compact difference scheme and the employed segregated solution solver are verified.

4.2 Mixed electroosmotic and pressure driven flow problem

Fig. 5 shows a schematic of the electroosmotic fluid flow bounded between two parallel planar plates (marked as electrodes). An external electric field has been applied across the right and left boundaries as shown in Fig. 5. Externally applied electric field interacts with the fluid inside the EDL, thereby leading to an electrokinetic body force or an electroosmotic force which acts on the bulk flow. As a result, fluid between two electrodes is set into motion. Under the approximation detailed in [21], the PNP equations

https://doi.org/10.4208/cicp.230914.040615a Published online by Cambridge University Press

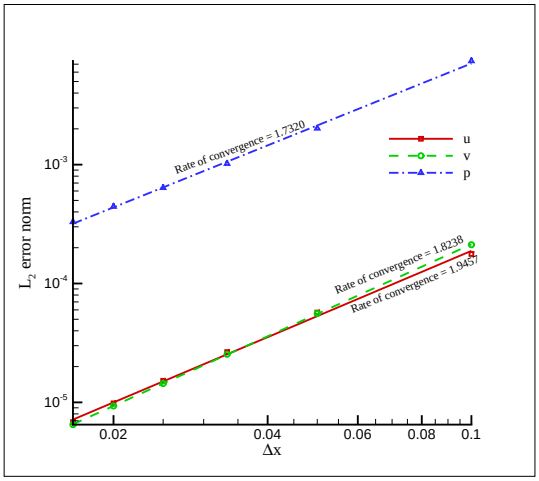


Figure 3: The computed spatial rates of convergence for u,v,p by solving the Navier Stokes equations, which are amenable to exact solutions.

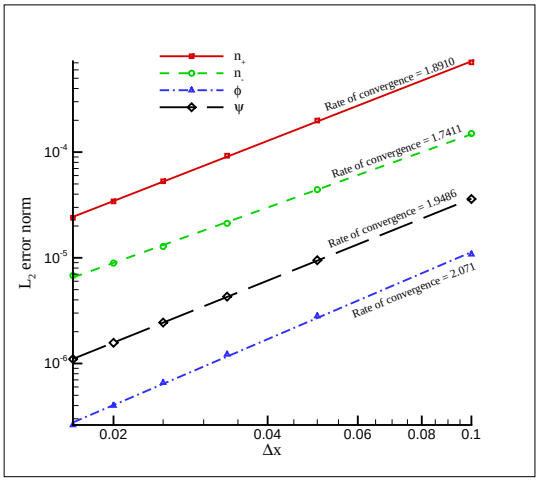


Figure 4: The computed spatial rates of convergence for n_+,n_-,ϕ and ψ by solving the PNP equations, which are amenable to exact solutions.

are simplified to the following two equations for a symmetric electrolyte

$$\frac{\partial p}{\partial x}=\frac{\partial^2 U}{\partial y^2}+\frac{\partial^2 \psi}{\partial y^2}, \tag{4.5}$$

$$\frac{\partial^2 \psi}{\partial x^2}+\frac{\partial^2 \psi}{\partial y^2}=\beta \sinh(\alpha\psi). \tag{4.6}$$

In the above, ψ denotes the normalized electroosmotic potential with respect to the zeta potential ζ_0. The ionic energy parameter α and the variable β shown in the Poisson-Boltzmann equation (4.6) are defined as $\alpha=ez\zeta_0/k_bT$ and $\beta=(\omega h)^2/\alpha$, where $\omega=1/\lambda=$

https://doi.org/10.4208/cicp.230914.040615a Published online by Cambridge University Press

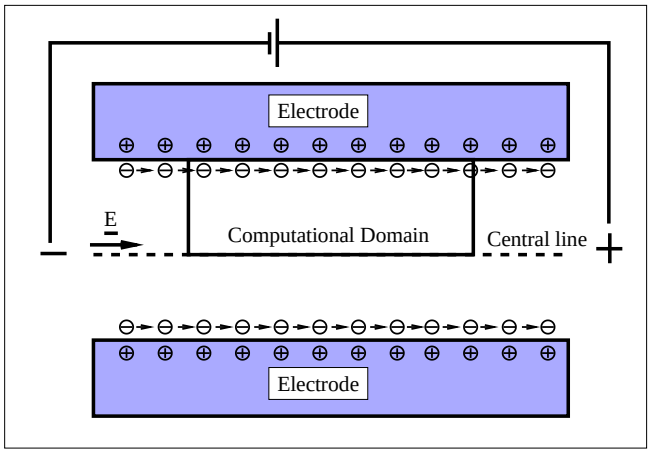


Figure 5: Schematic of the mixed electroosmotic and pressure driven flow problem described in Section 4.2.

$(\frac{8\pi n_0 e^2 z^2}{Dk_b T})^{1/2}$. Here the parameters e, z, k_b, T, h, λ, n_0 denote the electron charge, valence, Boltzmann constant, absolute temperature, characteristic length, Debye length and ion density, respectively.

The solution of the Poisson-Boltzmann equation (4.6) has been analytically derived by Burgreen and Nakache [22] for the specified values of α and β. The analytical solution for Eq. (4.6) is given below for $\alpha=1$ and $\beta=10^4$ [21] as,

$$\psi(y)=4\tanh^{-1}\left[\tanh\left(\frac{1}{4}\right)e^{-100(1-y)}\right]. \tag{4.7}$$

For the prescribed pressure gradient and the normalized electroosmotic potential $\psi(y)$, the ionized symmetric fluid flow velocity across the microchannel can be given as

$$u(y)=-\frac{1}{2}\frac{dp}{dx}\left(1-y^2\right)+1-\psi(y). \tag{4.8}$$

In this study, the complete set of the PNP equations is solved in the two-dimensional channel under the five specified pressure gradient values dp/dx ($=\chi=1,0.5,0,-0.5$ and -1). Thus the prescribed pressure gradient and the distribution of electroosmotic force in the domain as shown in Eq. (4.8) play a significant role in flow development. For this study, we have considered a square domain $0\le x,y\le 1$ which is divided into 41 grid points in each direction. The grid points are uniformly distributed in the x-direction while these points are clustered in the y-direction near the upper electrode. Calculations are preformed with a time step of 10^{-6}.

The predicted and the corresponding exact velocity profiles for different imposed pressure gradients χ are shown in Fig. 6. No-slip condition applied on the surface of the electrode at $y=1$ results in a boundary layer kind of sharp variation in the velocity profiles. For the negative pressure gradient cases ($\chi=-0.5$ and -1) flow experiences

https://doi.org/10.4208/cicp.230914.040615a Published online by Cambridge University Press

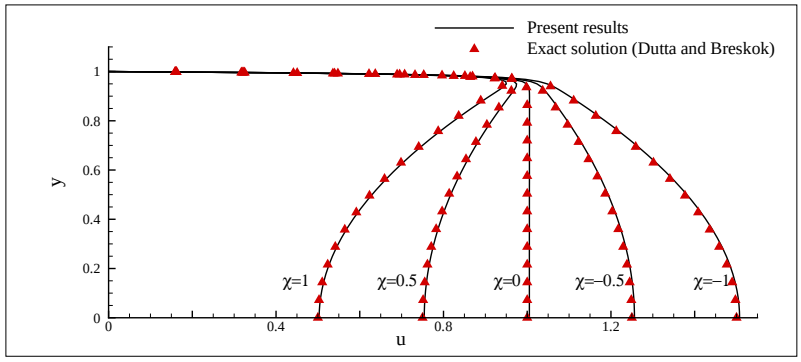


Figure 6: Comparison of the predicted and exact velocity profiles $u(y)$ at different streamwise pressure gradients for the mixed electroosmotic and pressure driven flow problem considered in Section 4.2.

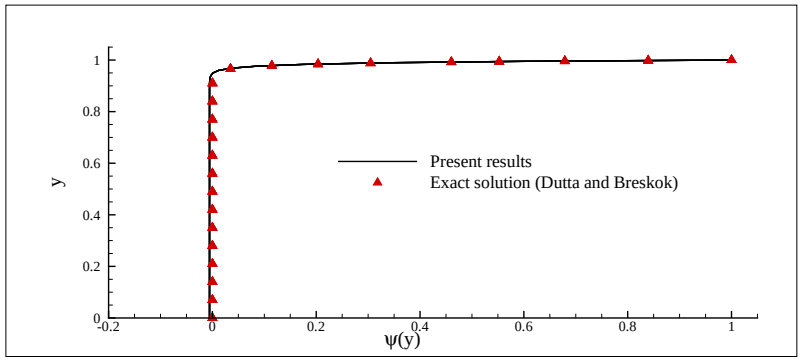


Figure 7: Comparison of the predicted and exact electric potentials $\psi(y)$ for the mixed electroosmotic and pressure driven flow problem considered in Section 4.2.

a favorable pressure gradient along the horizontal direction, causing therefore fuller velocity profiles. Flow for such case is very stable and less susceptible to separation and transition. In contrast, for the adverse pressure gradient case a considerable reduction in velocity is shown at $y=0$. Velocity profiles for the adverse pressure gradient cases show that such flows are susceptible to the applied or background disturbances and are therefore more unstable. In all of the cases, we observe a sharp variation in velocity profile near the top electrode $y=1$ which is essentially due to the dominant electroosmotic force in that region. This is also observed from the computed electric potential ψ profiles in Fig. 7. The effect of electroosmotic force decreases considerably away from the electrode and in that region the prescribed pressure gradient plays an important role in flow evolution.

The computed velocity profiles $u(y)$ in Fig. 6 corresponding to the different streamwise pressure gradients are all agreed well with the exact velocity profiles [21]. In Fig. 7, the computed electric potential ψ has an excellent agreement with the exact potential, given in [21], as well.

https://doi.org/10.4208/cicp.230914.040615a Published online by Cambridge University Press

4.3 Electroosmotic flow of Patankar and Hu [12]

Next, we consider the electroosmotic flow within two planar plates as shown in Fig. 8. Fluid flow has been subjected to the boundary conditions as shown in this schematic. This case has been investigated in [12]. PNP equations can be further simplified using the various assumptions listed in [12]. The resulting dimensionless equations for the EDL potential ψ and the electroosmotic velocity along the y-direction are as follows [12]

$$\frac{d^2\psi}{dy^2} = (\kappa h)^2 \psi, \tag{4.9}$$

$$\mathrm{Re}\frac{\partial u}{\partial t} = \frac{\partial^2 u}{\partial y^2} - (\kappa h)^2 \psi. \tag{4.10}$$

In the above, h, κ^{-1} and Re denote the channel width, Debye length, and Reynolds number, respectively. Here, the Reynolds number is defined as $Re = \rho \frac{\varphi \epsilon \zeta}{\mu H} \frac{h}{\mu}$, where ρ is the fluid density, μ the fluid viscosity, ζ the zeta potential and H the channel length.

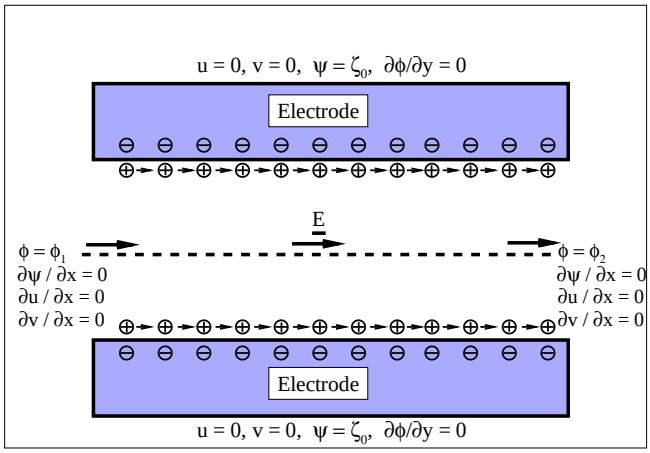


Figure 8: Schematic of the electroosmotic flow problem of Patankar and Hu [12] in Section 4.3.

In this example, the changes in velocity and electric potential profiles are studied for different Debye lengths $K = (\kappa h)^{-1}$ corresponding to the Reynolds number of 0.05. We compute numerical solutions at two different dimensionless Debye lengths K=15 and 25. A square domain $0 \le x,y \le 1$ has been considered. We have constructed a grid with 21×21 nodal points. The grid points are clustered near the electrodes in wall normal direction while we have distributed equi-spaced grid points along the electrodes. Calculations are preformed with a time step of 10^{-6}. Analytical solution of ψ can be derived as [12],

$$\psi(y) = \frac{\cosh[\,\kappa h(y-\frac{1}{2})\,]}{\cosh(\frac{\kappa h}{2})}. \tag{4.11}$$

https://doi.org/10.4208/cicp.230914.040615a Published online by Cambridge University Press

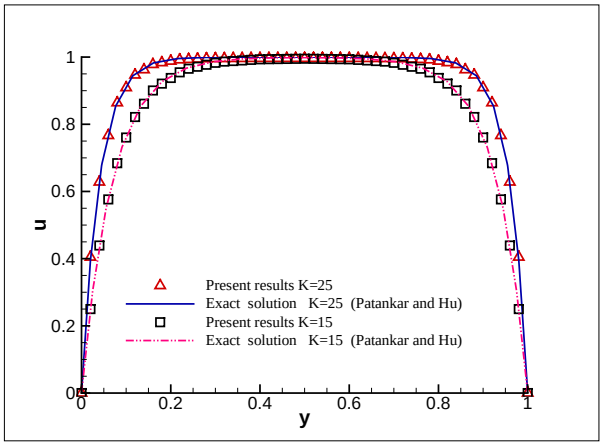


Figure 9: Comparison of the predicted and exact velocity profiles $u(y)$ at $K=15$ and 25 for the Patankar and Hu electroosmotic flow problem considered in Section 4.3.

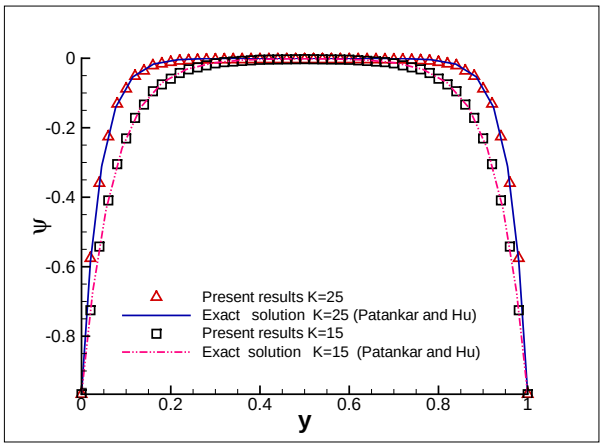


Figure 10: Comparison of the predicted and exact profiles of the electric potential ψ(y) for the electroosmotic flow problem of Patankar and Hu considered at $K=15$ and 25.

The steady-state solution for u has been derived as follows in [12] using the exact solution in Eq. (4.11)

$$u(y)=\frac{\cosh[\,\kappa h(y-\frac{1}{2})\,]}{\cosh(\frac{\kappa h}{2})}-1. \tag{4.12}$$

Fig. 9 compares the velocity profiles obtained for the Debye lengths of 15 and 25. An increase of the Debye length causes stronger interaction between the mobile charged particles and the surrounding fluid. This results in a higher Coulomb force, thereby causing a sharper velocity profile to develop for the $K=25$ case as compared to the case with $K=15$. Higher value of Debye length also results in steep profile for the electric potential as shown in Fig. 10. On the top and bottom electrodes, one observes the maximum

https://doi.org/10.4208/cicp.230914.040615a Published online by Cambridge University Press

magnitude of the electric potential which decreases rapidly in the wall normal direction. Thus, the induced Coulomb force is significant only in the small zone close to the electrode. Good agreement between the computed and the exact solutions can be clearly seen in Fig. 9 for the streamwise velocity profiles and in Fig. 10 for the electric potential. Thus, the proposed upwinding combined compact difference scheme and the developed flow solver provide consistent results for the coupled NS and PNP equations.

4.4 Electroosmotic flow due to the specified EDL potential and streamwise electric field

In this final verification study, we have considered a steady fully-developed electroosmotic flow in an open planar conduit. Uniform potentials $\psi_{u,w}$ and $\psi_{b,w}$ are applied at the top and bottom walls, respectively. Under the assumptions described in [23], the PNP equations derived in Section 2 can be further simplified to the following two dimensionless equations for ψ and U.

$$\frac{\partial p}{\partial x}=\frac{\partial^2 U}{\partial y^2}+\frac{\partial^2 \psi}{\partial y^2}, \tag{4.13}$$

$$\frac{\partial^2 \psi}{\partial x^2}+\frac{\partial^2 \psi}{\partial y^2}=\frac{1}{\lambda_D^2}\sinh(\psi). \tag{4.14}$$

In Eq. (4.14), λ_D $(=\lambda^*/H)$ denotes the dimensionless thickness and λ^* denotes the dimensional thicknesses of the Debye layer. Here, H is the characteristic length and we have chosen $\lambda_D=0.01$. The following exact solutions are derived at the prescribed value of pressure gradient $-\partial p/\partial x$ for Eqs. (4.13)-(4.14) in [23].

$$\psi(y)=4\tanh^{-1}\left[\tanh\left(\frac{\zeta_1}{4}\right)e^{\left(-\frac{1-y}{\lambda_D}\right)}\right]+4\tanh^{-1}\left[\tanh\left(\frac{\zeta_2}{4}\right)e^{\left(-\frac{1+y}{\lambda_D}\right)}\right], \tag{4.15}$$

$$u(y)=-\left[\psi(y)+\frac{\zeta_2-1}{2}y-\frac{\zeta_2+1}{2}\right]+\frac{y^2-1}{2}\frac{\partial p}{\partial x}. \tag{4.16}$$

In this study, the PNP equations have been solved subjected to the boundary conditions as shown in the schematic Fig. 11. At the upper wall, a fixed potential value $\psi_{u,w}=1$ has been prescribed. The effect of different potentials applied on the bottom wall $(\psi_{b,w}=-1,-0.5,0,0.5,1)$ on the development of velocity profiles has been studied here. Streamwise pressure gradient has been specified as $\partial p/\partial x=2$. We have considered a domain $0\le x\le 1$, $-1\le y\le 1$. A grid with 31×31 nodal points has been constructed. These grid points are clustered near the electrodes in wall normal direction while we have used equi-spaced grid points along the parallel electrodes. Calculations are preformed with a time step of 10^{-7}. Fig. 12 shows that the combination of the adverse pressure gradient and negative wall potential leads to the formation of inflection point in the velocity profile. As one applies a higher positive potential at the bottom wall, tendency of flow reversal is reduced. However, flow velocity in the central region of the domain has been

https://doi.org/10.4208/cicp.230914.040615a Published online by Cambridge University Press

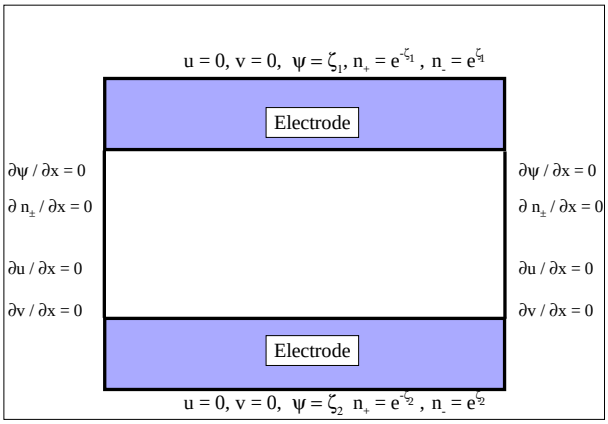


Figure 11: Schematic of the electroosmotic flow due to the specified EDL potential and the streamwise electric field.

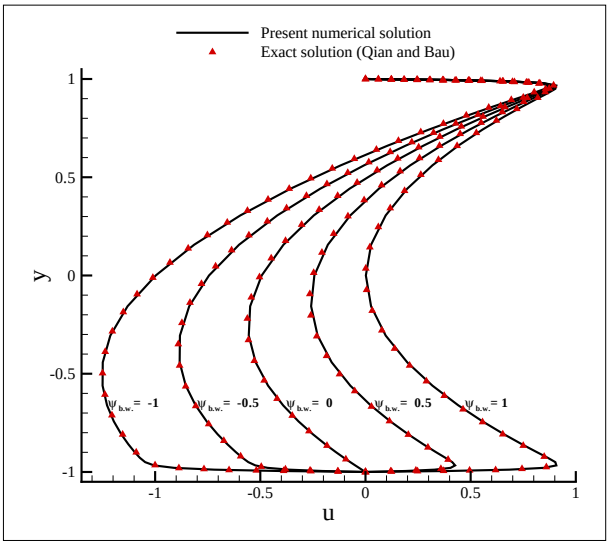


Figure 12: Comparison of the predicted and exact profiles $u(y)$ at different values of $\psi_{b,w}$ for the electroosmotic flow generated by the specified EDL potential and the streamwise electric field.

severely affected due to the significant adverse pressure gradient. Velocity profiles predicted at different potentials applied on the bottom wall in Fig. 12 and the profiles of ψ in Figs. 13 and 14 show good match with the analytical solutions.

5 Numerical results

After verifying the proposed scheme and the incompressible flow solver, we obtain important physical details about the electroosmotic flow development in two different channel geometries. The electroosmotic flow between two parallel planar plates is investi-

https://doi.org/10.4208/cicp.230914.040615a Published online by Cambridge University Press

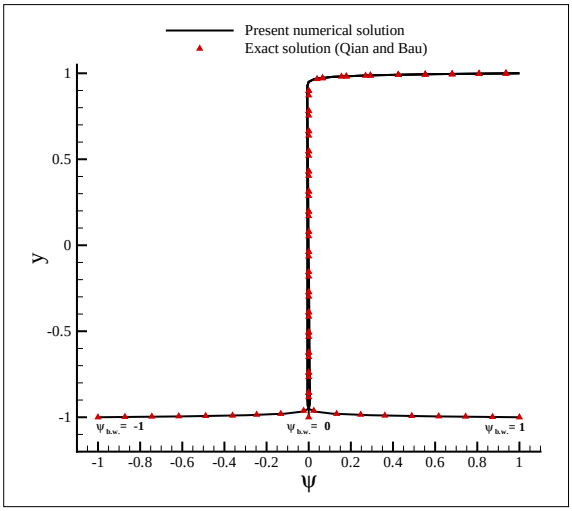


Figure 13: Comparison of the predicted and exact electric potential profiles for the cases investigated at $\psi_{b,w}$= -1, 0, 1.

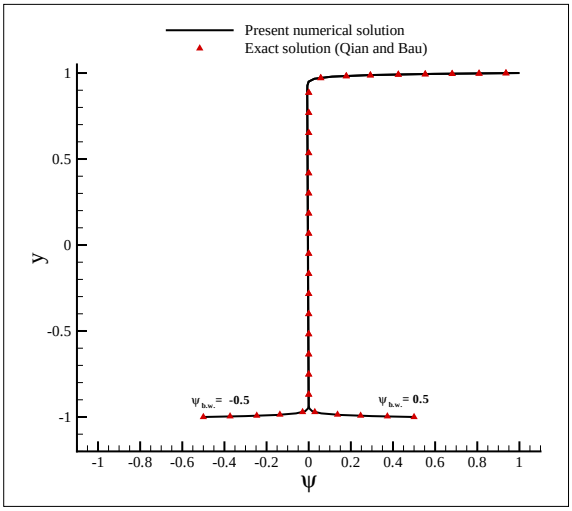


Figure 14: Comparison of the predicted and exact electric potential profiles for the cases investigated at $\psi_{b,w}$ = -0.5, 0.5.

gated first in Section 5.1. In Section 5.2 the electroosmotic flow inside a wavy channel has been considered.

5.1 Electroosmotic flow between two parallel plates

The electroosmotic flow inside a parallel channel with the planar upper and lower plates separated by a distance $h=2\times10^{-5}$m has been investigated. Schematic of the problem along with the boundary conditions is shown in Fig. 15. Eqs. (2.18)-(2.23) are solved at

https://doi.org/10.4208/cicp.230914.040615a Published online by Cambridge University Press

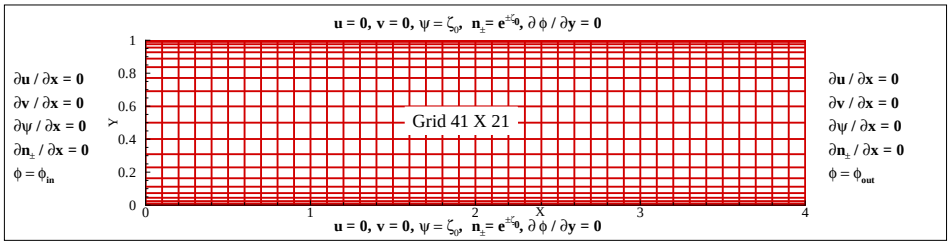


Figure 15: The specified boundary conditions and mesh distribution for solving the electroosmotic flow in a straight and parallel channel.

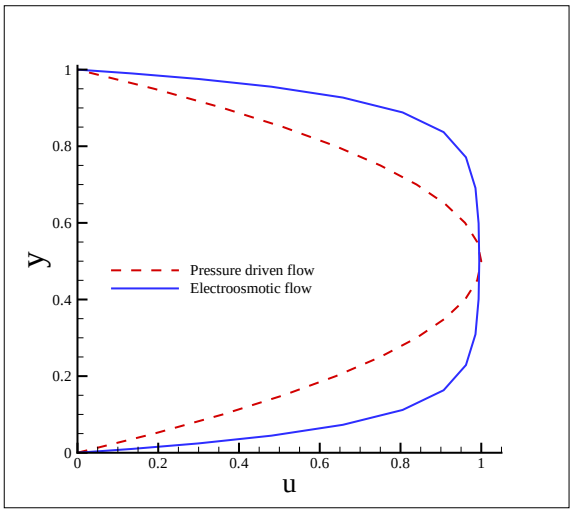


Figure 16: Comparison of the velocity profiles in a parallel channel under different driven forces.

ρ=1000kg/m^3, μ=0.91$\times10^{-3}Ns/m^2$, T_0=300K, z=1, ϵ=80, ζ_0=$-$25mV, n_0=3$\times10^{19}m^{-3}$, λ_D=1.38$\times10^{-6}m$. The physical domain is a rectangle with the dimensionless length of 4 and height of 1, where the characteristic distance is h=2$\times10^{-5}$m. Given the characteristic length and velocity, which is $U_0=-\epsilon\epsilon_0\zeta_0 Ex/\mu$ [21], the Reynolds number Re ($\equiv\rho U_0 h/\mu$) and K ($\equiv h/\lambda_D$) turn out to be 0.05 and 15, respectively. In the above expression the parameter Ex indicates the externally applied electric field.

Simulations are performed in a mesh with 41$\times$21 grid points as shown in Fig. 15. One of the main motivations behind the present study is to reveal the difference between the pressure-driven and the electroosmotic force-driven flowfields. Due to the prescribed inlet and outlet boundary conditions, flow eventually achieves steady state. In Fig. 16, the velocity profile obtained for the pressure-driven flow has been compared with that for electroosmotic flow. One can observe a parabolic kind of profile for the pressure driven case. In contrast, for the electroosmotic flow case the velocity profile is much sharper with a fully developed kind of variation due to dominant Coulomb force near the top and bottom walls. The velocity profile in electroosmotic flow also suggests that there is

https://doi.org/10.4208/cicp.230914.040615a Published online by Cambridge University Press

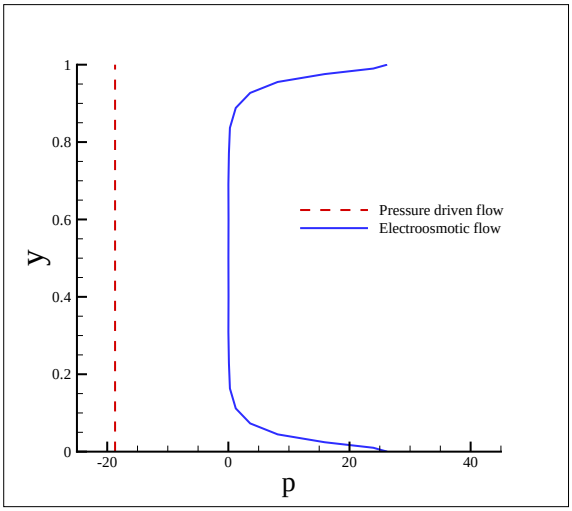


Figure 17: Comparison of the pressures in a parallel channel under different driven forces.

an increased mass flow due to the action of Coulomb force as compared to the pressure driven flow case. Thus apart from controlling flow instabilities, one can control the net mass flux as well in electroosmotic flow case.

In Fig. 17, one can observe that the pressure across the channel almost remains unchanged for the pressure-driven flow case. In contrast, a sharply varying pressure is observed near the walls for the electroosmotic flow case. This is essentially due to the coupling between Navier-Stokes and PNP equations. Higher Coulomb force near the top and bottom walls changes the overall velocity as well as the pressure field itself.

The dominant nature of Coulomb force near the top and bottom walls can be also observed from the predicted profiles of $n_+(y)$, $n_-(y)$, ψ and Φ in Fig. 18. Since we have applied negative zeta potential at the electrodes, accumulation of large positive ions n_+ near the top and the bottom boundaries is observed. Subsequently, the concentration of positive ions reduces in regions away from the walls. In contrast, there is a higher concentration of negative ions $n_-(y)$ in the central region $(y=0.50)$ of the domain. This concentration reduces as we approach the top and bottom walls. Similarly, electric potential (ψ) due to the charges attached to the wall and due to externally applied electric field vary significantly near the top and bottom walls.

Based on the computed solutions, the force vectors are plotted in Fig. 19. The predicted magnitudes of force vectors indicate that the Coulomb force is dominant near the wall. In contrast to the classical incompressible viscous channel flow, the predicted force vectors point towards the no-slip channel walls due to the Coulomb force pointing towards the lower and upper walls. Thus the Coulomb force can significantly reduce the tendency of flow to undergo flow separation. This also highlights the stabilizing nature of the additionally introduced Coulomb force via the coupled Navier-Stokes and PNP equations.

https://doi.org/10.4208/cicp.230914.040615a Published online by Cambridge University Press

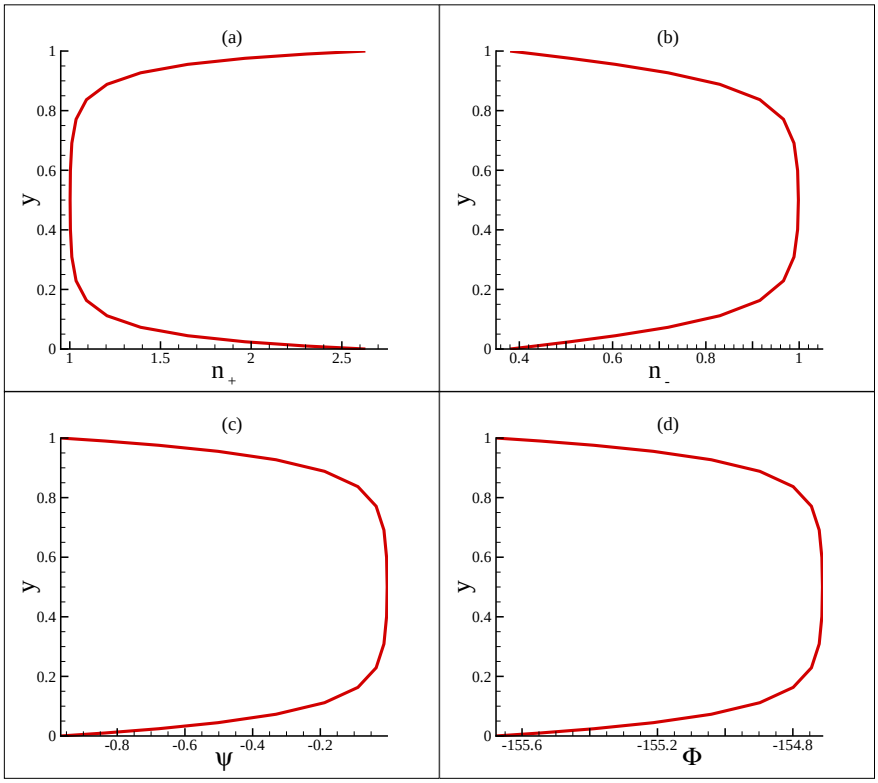


Figure 18: The predicted profiles of $n_{\pm}$, ψ and Φ are plotted with respect to y. (a) n_{+}; (b) n_{-}; (c) ψ; (d) Φ.

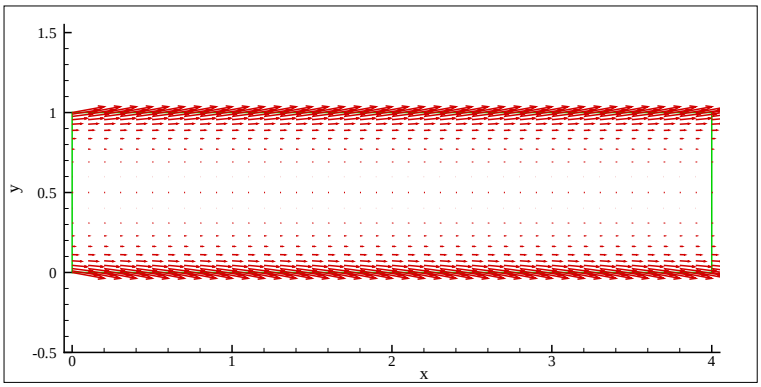


Figure 19: The predicted electroosmotic force vector in the investigated straight channel.

In Fig. 20, different forces which play an active role in the flow development inside the straight channel are compared. Coulomb force resulting from the externally applied electric field plays a dominant role, as shown in Fig. 20, thereby causing the steeper velocity profile, as shown in Fig. 16, to develop. However, this force is dominant only near the top

https://doi.org/10.4208/cicp.230914.040615a Published online by Cambridge University Press

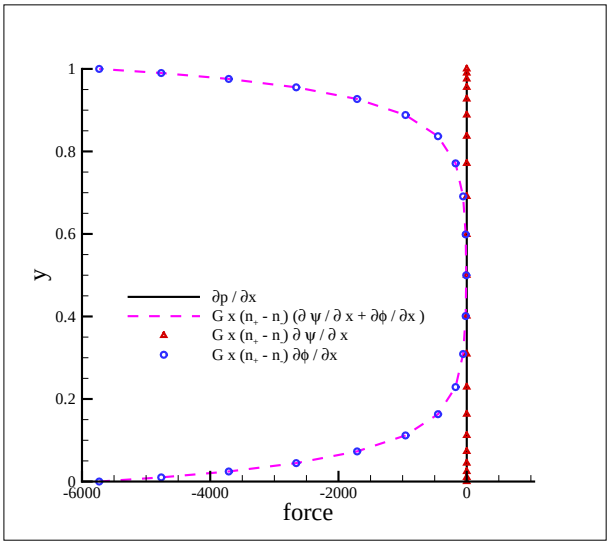


Figure 20: Comparison of the Coulomb and pressure gradient forces at $x=2$ in a straight channel.

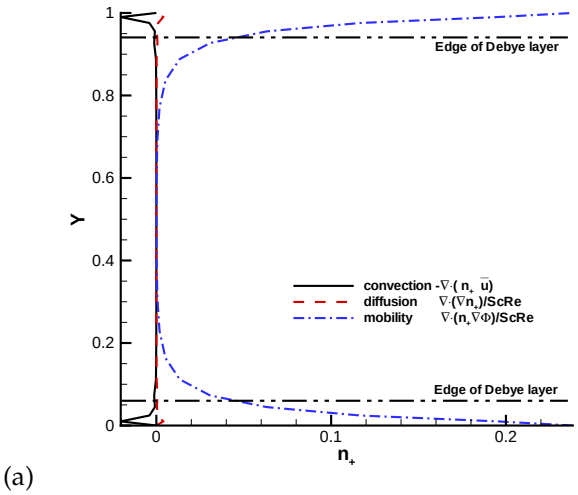
and bottom walls. As noted earlier, the total electric potential can be summed up as the potential due to charge attachment to electrodes and the potential due to external electric field. In Fig. 20, we have shown the resultant force variation due to these individual potentials. Fig. 20 shows that the pressure gradient force $-\partial p/\partial x$ and the Coulomb force due to zeta potential are both negligibly small. However, the externally applied electric field plays a significant role in Coulomb force formation and it significantly controls the flow development near the parallel walls.

Comparison of the convective flux, diffusive flux, and migration flux is shown in Fig. 21 for positive and negative ions. For n_+, the electromigration flux dominates near the two negatively-charged planar plates. In contrast, for negative charge the negative-valued diffusive flux dominates the convection and mobility fluxes. Since the planar walls are negatively charged, electromigration flux increases sharply in the direction approaching lower and upper walls. The electromigration flux for the negative ion has a mild variation near the electrodes. The edge of Stern layer and the predicted diffuse and boundary layers are also plotted in Fig. 22 for providing a clear picture of all the important layers formed near the channel walls.

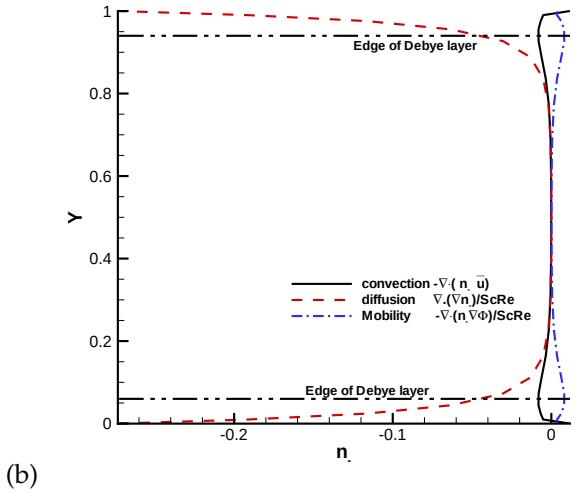
5.2 Electroosmotic flow between two wavy plates

Schematic of the electroosmotic flow in the wavy channel is shown in Fig. 23. This case has been investigated under the similar conditions as described in Section 5.1. For the comparison sake, velocity, pressure, pressure gradient and the Coulomb force resulting from the formation of zeta potential are plotted at the three different streamwise planes $x=1.2$, 2 and 2.8. Note that the wavy channel surface imposes a continuously varying

https://doi.org/10.4208/cicp.230914.040615a Published online by Cambridge University Press



(a)



(b)

Figure 21: Comparison of the predicted profiles of $-\bigtriangledown\cdot n_{\pm}\underline{u}$, $\bigtriangledown\cdot(\bigtriangledown n_{+})/ScRe$ and $\bigtriangledown\cdot(n_{+}\bigtriangledown\Phi)/ScRe$ for ions n_{+} and n_{-} in a straight channel. (a) positive ion; (b) negative ion.

pressure gradient as fluid flows inside the channel. This results in a continuous variation either in velocity or in pressure field inside the channel. Fig. 24 shows the profiles of streamwise velocity component $u(x,y)$, transverse velocity component $v(x,y)$ and pressure $p(x,y)$ at $x=1.2$, 2 and 2.8. For the purpose of illustrating the wall effects on flow development, the solution obtained in planar channel is also plotted in the same figure. The symmetric nature of the u-velocity profile observed for the case of flow inside a planar channel is lost in the case of flow inside a wavy channel.

The wavy configuration of the channel imposes a spatially varying pressure field in

https://doi.org/10.4208/cicp.230914.040615a Published online by Cambridge University Press

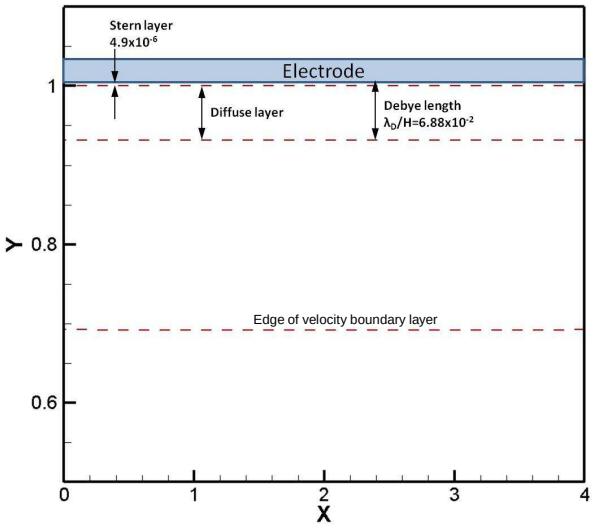


Figure 22: The predicted edges of the diffuse layer, velocity boundary layer and Debye layer.

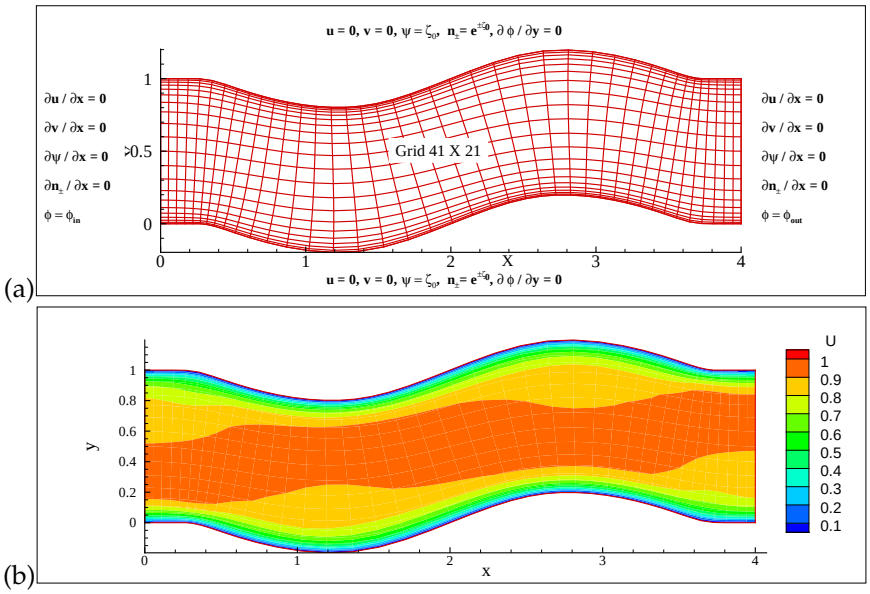


Figure 23: (a) The specified boundary conditions and mesh point distribution for solving the electroosmotic flow problem in wavy channel; (b) The predicted velocity contours in a wavy channel.

the complete domain, thereby causing flow acceleration as well as flow retardation to occur in different parts of the domain. Thus in case of electroosmotic flow inside a wavy channel, in addition to the Coulomb force there is a significant favorable or adverse pressure gradient force present at different sections of the wavy channel.

https://doi.org/10.4208/cicp.230914.040615a Published online by Cambridge University Press

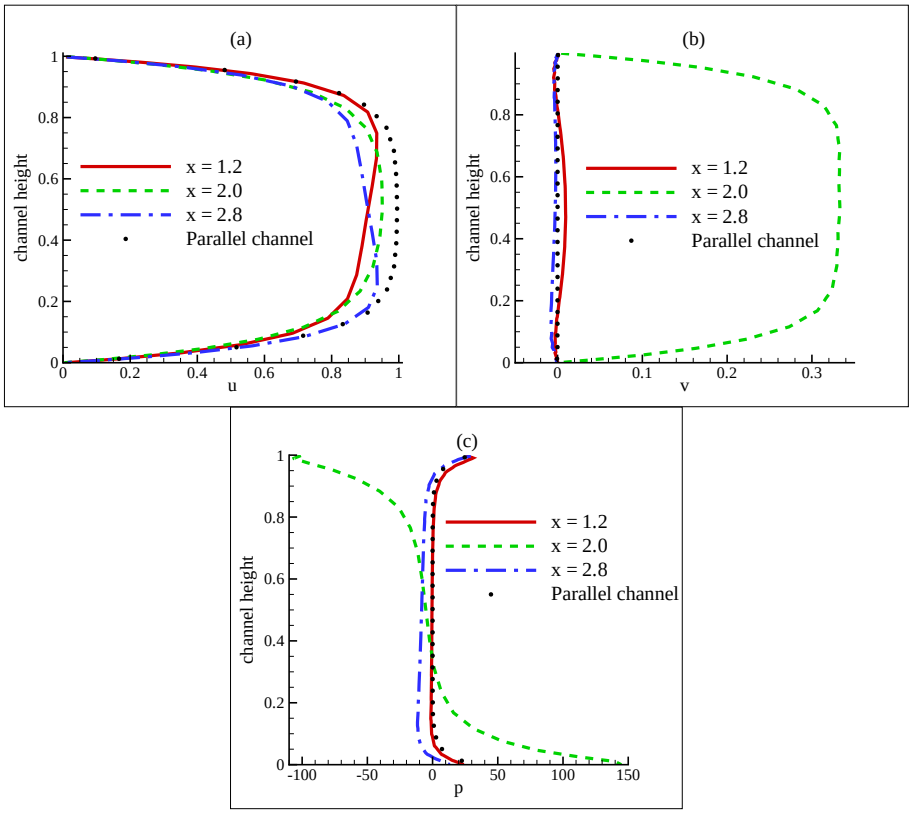


Figure 24: Comparison of the velocity and pressure profiles in parallel and wavy channels. (a) velocity u; (b) velocity v; (c) pressure p.

Like the case predicted in the planar channel, the Coulomb force is prevailing near the upper and lower walls. Also, the force vectors plotted in Fig. 25 point towards the walls. The negative v-velocity profiles in Fig. 24 (b) is also observed near the wall. In the region between the cross-sections $x=2$ and $x=3$ on the top wavy wall, one can observe that surface curvature causes a strong adverse pressure gradient to develop. However, the distribution of velocity vectors shows reduced tendency to undergo flow separation due to the effective Coulomb force near the walls.

At the three chosen streamwise locations, we plot as before the forces leading to flow motion in wavy channel. In Figs. 26, 27, 28, the dominant force is the Coulomb force near, in particular, the walls rather than the pressure gradient force. In these figures, one can also observe that the Coulomb force generated from the externally applied electric field dominates the force resulting from the formation of zeta potential at all the three chosen streamwise planes. In all of the cases, dominant Coulomb force generated from the externally applied electric field exhibits an almost symmetric variation across different cross-sections of the wavy channel. However, the imposed favorable or adverse pressure gradient due to wavy surface causes an unsymmetrical variation of velocity profile

https://doi.org/10.4208/cicp.230914.040615a Published online by Cambridge University Press

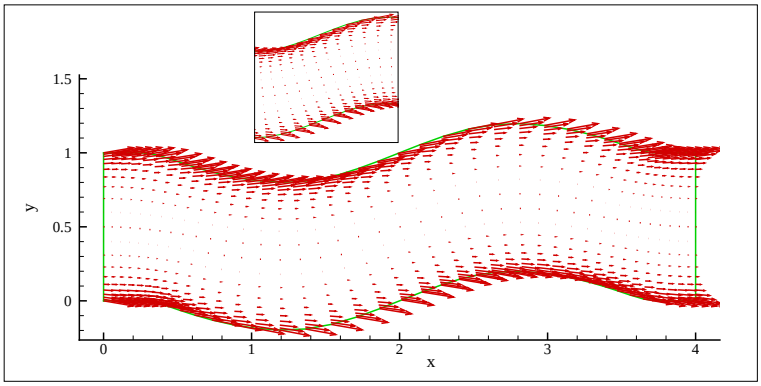


Figure 25: The predicted force vector plots in the investigated wavy channel.

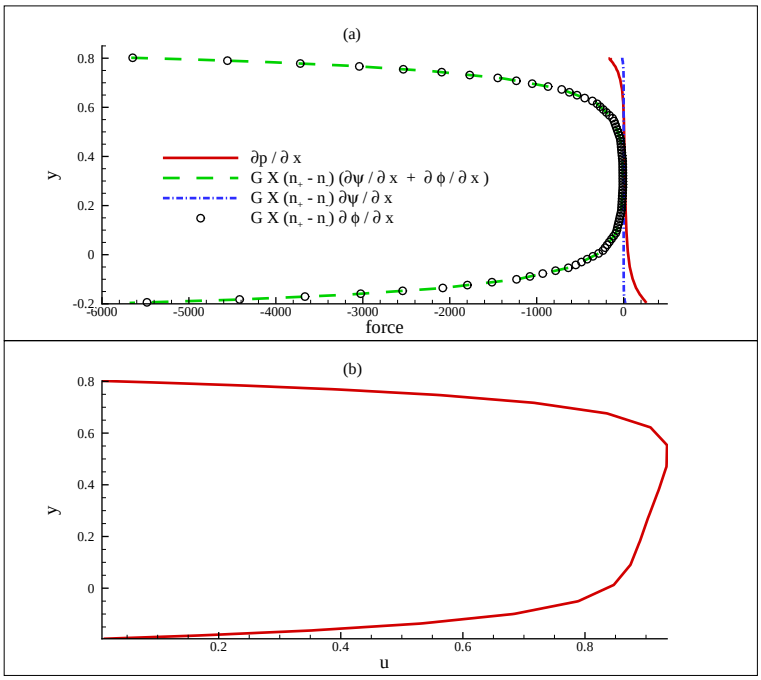


Figure 26: (a) Comparison of forces; (b) velocity profile u ($x=1.2$) in the investigated wavy channel.

to develop. For example, before reaching the location $x=1.2$, flow on the lower wall experiences adverse pressure gradient while on the top wall flow experiences favorable pressure gradient. This asymmetrically imposed pressure gradient causes flow acceleration on the top surface and flow retardation on the bottom surface. This is observed in the velocity profile at $x=1.2$ as shown in Fig. 26. Similarly, one can explain variations in the velocity profiles at locations $x=2$ and $x=2.8$ in Figs. 27, 28.

One can also observe from Fig. 29 that the Coulomb force generated by zeta potential as well as the pressure gradient force are responsible for the asymmetric force distribution

https://doi.org/10.4208/cicp.230914.040615a Published online by Cambridge University Press

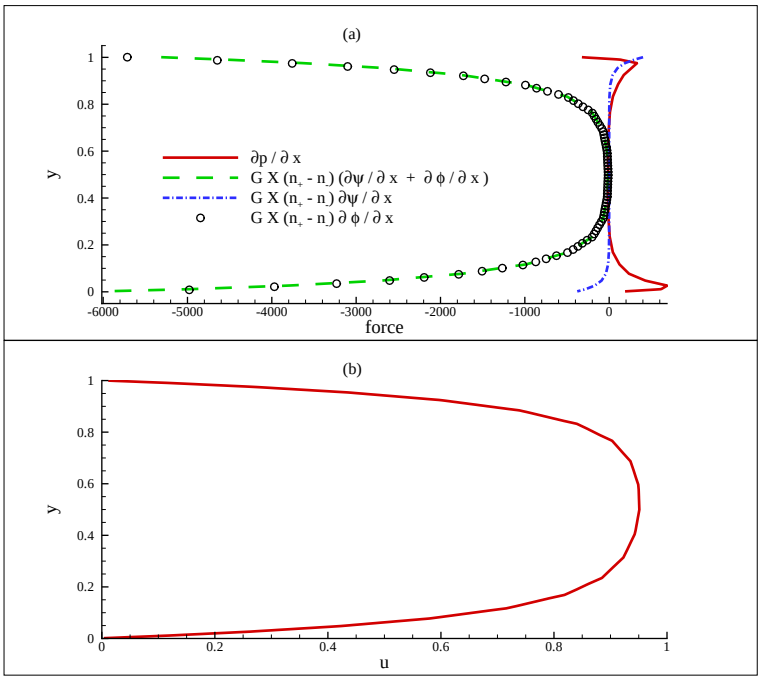


Figure 27: (a) Comparison of forces; (b) velocity profile u ($x=2$) in the investigated wavy channel.

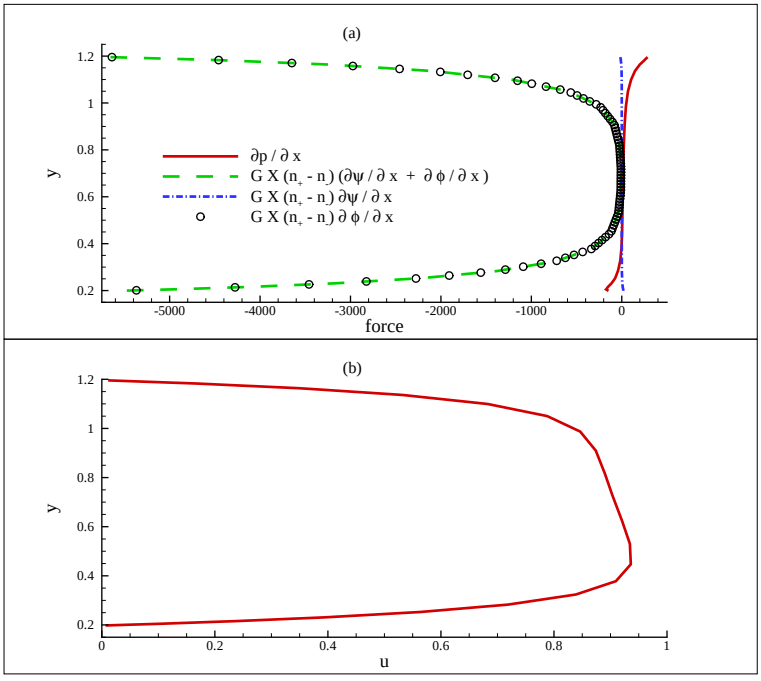


Figure 28: (a) Comparison of forces; (b) velocity profile u ($x=2.8$) in the investigated wavy channel.

https://doi.org/10.4208/cicp.230914.040615a Published online by Cambridge University Press

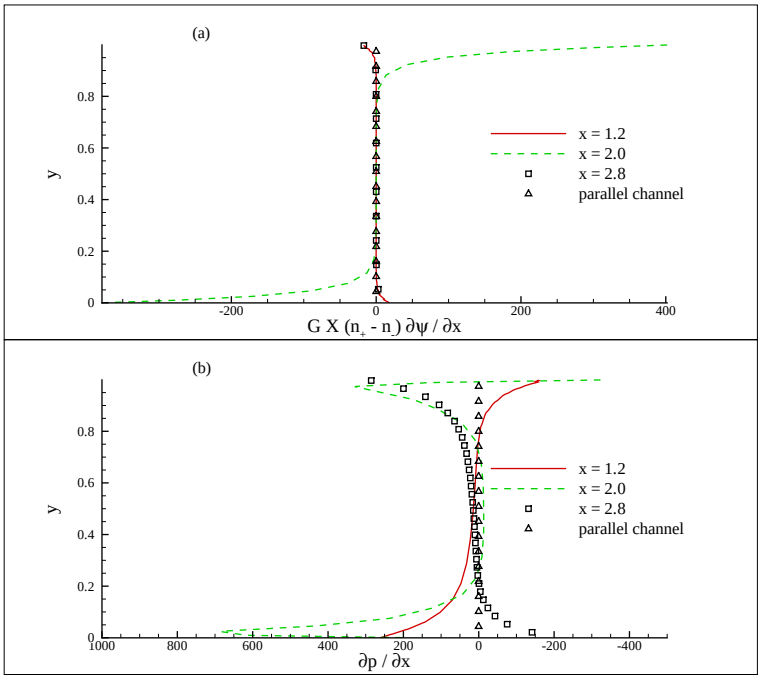


Figure 29: Comparison of the Coulomb and pressure gradient forces in the investigated wavy channel. (a) Coulomb forces generated by the zeta potential; (b) profiles of the pressure gradient force in x direction.

inside wavy channel. For the case of electroosmotic flow inside a plane channel, the imposed pressure gradient is zero while in the case of wavy channel, imposed pressure gradient sharply varies near the top and bottom surfaces.

In the end, relative significance of the velocity and concentration profiles has been shown in Fig. 30 for the problem discussed in Section 5.1. Fig. 30 shows that the concentration profiles have much sharper variation as compared to the boundary layer profiles while the profiles for the zeta potential and electric potential have similar variation. For the negatively charged top and bottom surfaces, there is a sharper variation of the n_+ ion profile as compared to the profile for the n_- ion.

6 Concluding remarks

In this study we have investigated the motion of an electroosmotic flow bounded by the negatively charged upper and lower plates by solving a set of differential equations composed of the Poisson-Nernst-Planck equations and the nonlinear incompressible Navier-Stokes equations. Due to the near-wall sharply varying velocity profile caused by an externally applied electric field, the combined compact difference scheme which yields sixth-order accuracy for the diffusion (or second-order derivative) terms and seventh-order accuracy for the convection (or first-order derivative) terms is developed in a stencil

https://doi.org/10.4208/cicp.230914.040615a Published online by Cambridge University Press

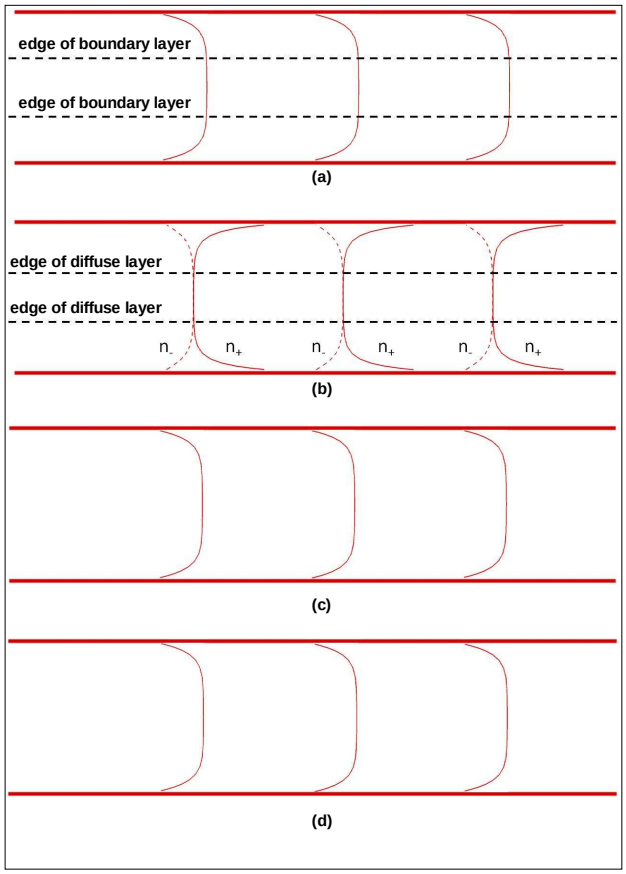


Figure 30: The predicted profiles of problem 5.1. (a) velocity profiles; (b) concentration profiles; (c) profiles of ψ; (d) profiles of Φ.

of five grid points. For enhancing convective numerical stability and improving dispersive accuracy, the method underlying the minimization of numerical wavenumber error is adopted to develop the upwinding combined compact difference scheme. Without introducing any flux or slope limiter into the scheme development, we still can resolve high gradient solution profile near the wall without exhibiting unphysical oscillations.

The proposed scheme for approximating the spatial derivative terms and the developed incompressible Navier-Stokes flow solver based on the pressure-velocity coupling DFC method are used to solve the model problems amenable to analytical solutions. This computationally verified code developed for solving the coupled PNP and NS equations is subsequently applied to solve the electroosmotic flow inside planer and wavy channels. The transport phenomena of charges in both channels are investigated with the emphasis on investigating the roles of diffusion and electromigration terms leading to flow motion. In addition, the relative significance of the different forces arising from the pressure gradient, viscous diffusion and Coulomb force terms in flow development has

https://doi.org/10.4208/cicp.230914.040615a Published online by Cambridge University Press

been also discussed. The effect of channel curvature on electroosmotic flow motion in the wavy channel is also studied here.

In the present analysis of electroosmotic flowfields in plane as well as wavy channels, we conclude that the electroosmosis process can be used as an effective way to control fluid flow inside micro-channels. The additional Coulomb force resulting in this process dominates near the electrode surfaces and significantly controls flow development.

References

[1] K. F. Jensen, Microchemical systems; status, challenges, and opportunities, *AIChE J.*, 45, 1999, 2051-2054.
[2] A. Manz, N. Graber, H. M. Widmer, Miniaturized total chemical-analysis systems: A novel concept for chemical sensing. Sensors Actuators, *B-Chemical*, 1(1-6): 244-248, 1990.
[3] D. R. Reyes, D. Lossifidis, P. A. Auroux, A. Manz, Micro total analysis systems, I. Introduction, theory, and technology, *Anal. Chem.*, 74, 2623-2636, 2002.
[4] J. Cao, P. Cheng, F. J. Hong, Applications of electrohydrodynamics and Joule heating effects in microfluidic chips: A review, *Science in China Series E: Technological Sciences*, vol. 52(12), 3477-3490, 2009.
[5] T. M. Squires, M. Z. Bazant, Induced-charge electroosmosis, *J. Fluid Mech.*, 2004, 509: 217-252.
[6] R. F. Probstein, Physiochemical Hydrodynamics, *John Wiley and Sons, New York*, 1994.
[7] A. Castellanos, Electrohydrodynamics, *New York: Springer Wien*, 1998.
[8] D. J. Griffiths, Introduction to Electrodynamics. *NJ: Prentice Hall*, 1999.
[9] A. Ramos, H. Morgan, N. G. Greenetal., AC electrokinetics: A review of forces in microelectrode structures, *J. Phys D: Appl. Phys.*, 1998, 31(18): 2338-2353.
[10] D. Q. Li, Electrokinetics in Microfluidics, *New York: Academic Press*, 2004.
[11] J. R. Melcher, G. I. Taylor, Electrohydrodynamics: A review of the role of interfacial shear stresses, *Annu. Rev. Fluid Mech.*, 1, 111-146, 1969.
[12] N. A. Patankar, H. H. Hu, Numerical simulation of electroosmotic flow, *Anal. Chem.*, 1998, 70, 1870-1881.
[13] P. H. Chiu, T. W. H. Sheu, On the development of a dispersion-relation-preserving dual-compact upwind scheme for convection-diffusion equation, *J. Comput. Phys.*, 228, 2009, 3640-3655.
[14] C. K. W. Tam, J. C. Webb. Dispersion-relation-preserving finite difference schemes for computational acoustics. *J. Comput. Phys.*, 1993, 107, 262-281.
[15] R. W. Johnson, R. J. Mackinnon, Equivalent versions of the QUICK scheme for finite-difference and finite-volume numerical methods, *Commun. Appl. Numer. Methods*, 8, 1992, 841-847.
[16] T. K. Sengupta, High Accuracy Computing Methods: Fluid Flows and Wave Phenomena, Cambridge Univ. Press., New York, USA, 2013.
[17] T. K. Sengupta, A. Dipankar, P. Sagaut, Error dynamics: Beyond von Neumann analysis, *J. Comput. Phys.* 226 (2007),1211-1218.
[18] T. K. Sengupta, G. Ganeriwal, S. De, Analysis of central and upwind schemes, *J. Comput. Phys.*, 192 (2003), 677-694.
[19] T. K. Sengupta, V. Lakshmanan, V. V. S. N. Vijay, A new combined stable and dispersion relation preserving compact scheme for non-periodic problems, *J. Comput. Phys.* 228 (2009), 3048-3071.

https://doi.org/10.4208/cicp.230914.040615a Published online by Cambridge University Press

[20] T. W. H. Sheu, P. H. Chiu, A divergence-free-condition compensated method for incompressible Navier-Stokes equations, *Comput. Methods Appl. Mech. Engrg.*, 196, 2007, 4479-4494.
[21] P. Dutta, A. Breskok, Analytical solution of combined electroosmotic/pressure driven flows in two-dimensional straight channels: Finite Debye layer effects, *Anal. Chem.*, 2001, 73, 1979-1986.
[22] D. Burgreen, F. R. Nakache, Electrokinetic flow in ultrafine capillary slits, *J. Phy. Chem.*, 1964, 68(5), 1084-1091.
[23] S. Qian, H. H. Bau, Theoretical investigation of electro-osmotic flows and chaotic stirring in rectangular cavities, *Appl. Math. Modelling*, 29 (2005), 726-753.

https://doi.org/10.4208/cicp.230914.040615a Published online by Cambridge University Press